

# Impact of geodetic information, subduction zone segmentation and slow-slip events in probabilistic seismic hazard: a case study for Costa Rica

Mario Arroyo-Solórzano<sup>1,2</sup>, Jorge Jara<sup>1</sup>, Graeme Weatherill<sup>1</sup>, Álvaro González<sup>1,3</sup>, Diego A. Hidalgo-Leiva<sup>1,4</sup> and Fabrice Cotton<sup>1,2</sup>

<sup>1</sup>GFZ Helmholtz Centre for Geosciences, Telegrafenberg, 14473 Potsdam, Germany, E-mail: [marroyo@gfz.de](mailto:marroyo@gfz.de).

<sup>2</sup>Institute of Geosciences, University of Potsdam, 14476 Potsdam, Germany

<sup>3</sup>Centre de Recerca Matemàtica, 08193 Bellaterra, Barcelona, Spain

<sup>4</sup>Earthquake Engineering Laboratory, University of Costa Rica, 1501-2060 San Pedro, San José, Costa Rica

Accepted 2025 May 30. Received 2025 May 9; in original form 2024 November 29

## SUMMARY

A slow-slip event (SSE) is a slow release of tectonic stress along a fault zone, over periods ranging from hours to months. SSEs have been recorded in most of the geodetically well-instrumented subduction zones. Although these transient events observed by geodesy are typically excluded from probabilistic seismic hazard analysis (PSHA), they might play a crucial role in the seismic cycle by reducing the seismic slip rate (slip rate discounting the aseismic process). This effective reduction implies that incorporating SSEs into PSHA may improve the reliability of hazard assessments. Costa Rica, located at the southern end of the Middle American Trench, hosts large earthquakes as well as SSEs. Shallow and deep SSEs have long been detected at the Nicoya peninsula, in northern Costa Rica, and recently, also in the southern part of the country at the Osa peninsula. In this study, we first collect geodetic and SSE observations in Costa Rica. Then, we propose a method to incorporate them into PSHA, based on identifying regions where SSEs occur, inferring slip deficits and estimating seismic slip rates in each subduction segment. Next, we analyse the implications for PSHA and its epistemic uncertainty, using these seismic slip rates, the resulting seismic moment rate budgets, and determining earthquake rates and maximum magnitudes with different approaches. Finally, we compute a countrywide PSHA following the 2022 Costa Rica Seismic Hazard Model (CRSHM 2022) but modifying the seismic source characterization using geodetic information for the regions where SSEs occur. Compared to the CRSHM 2022, this approach leads to reductions of the resulting peak ground acceleration at return period of 475 yr (PGA-475) of up to ~15 per cent in the Nicoya peninsula, but also to an increase up to ~40 per cent in the Central Pacific region and ~30 per cent in the Osa peninsula. Moreover, we find that, under a geodetic-based approach and disregarding SSEs, the PGA-475 would increase by up to ~10 per cent. Our novel approach underscores the relevance of incorporating geodetic observations and particularly SSEs into PSHA, especially in subduction margins near the coast.

**Key words:** Plate motions; Seismic cycle; Transient deformation; Earthquake hazards; Earthquake source observations; Subduction zone processes..

## 1 INTRODUCTION

The evolution of geodetic networks has increased the monitoring of crustal deformation worldwide. Such observations have highlighted the importance of identifying and characterizing aseismic processes for quantifying seismic potential (Avouac 2015; Jolivet & Frank 2020). In subduction zones, the convergence rate is accommodated

through various processes, including intraplate deformation, regular earthquakes, and aseismic transients, among others (Radiguet *et al.* 2012; Bürgmann & Thatcher 2013; Bürgmann 2018). Some of the most relevant aseismic processes are the slow-slip events (SSEs), fault slip events that slowly release tectonic stress over hours to months, often accompanied by seismic tremors and low-frequency earthquakes (Obbara & Kato 2016; Kano *et al.* 2018;

Weng & Ampuero 2022; Nishikawa *et al.* 2023). SSEs occur in most subduction zones, representing a crucial element to be considered in seismic hazard (Obara & Kato 2016; Dascher-Cousineau & Bürgmann 2024).

In subduction zones, SSEs occur mostly in the deep plate interface (30–40 km), or in the shallow part (<10 km), usually avoiding the megathrust seismogenic depth (Bürgmann 2018). However, some studies suggest the connection of the SSEs with the megathrust area (Radiguet *et al.* 2011, 2012; Obara & Kato 2016; Uchida *et al.* 2016; Saux *et al.* 2022). Moreover, SSEs typically occur in subduction patches characterized by abundant water and near-lithostatic pore-fluid pressure (Bürgmann 2018; Nishikawa *et al.* 2019), mostly in areas with intermediate coupling along young, warm subduction zones such as Cascadia, Nankai, Japan, Mexico, Costa Rica, New Zealand, Chile and Peru (Wallace *et al.* 2016; Ozawa 2017; Plata-Martinez *et al.* 2021; Jara *et al.* 2024). SSEs present high sensitivity to external stress perturbations with three possible interactions (1) between different SSEs, (2) between SSEs and small earthquakes and (3) between SSEs and large earthquakes; this last one being the most relevant for seismic hazard (Obara & Kato 2016). In this regard, SSE migration patterns have been suggested as precursors of large seismic ruptures like the 2011 Tohoku-Oki earthquake in Japan, the 2014 Guerrero earthquake in Mexico, and the 2014 Iquique earthquake in Chile, among others (Ruiz *et al.* 2014; Cruz-Atienza *et al.* 2021; Nishikawa *et al.* 2023).

Consequently, SSEs are an important part of the seismic cycle, but their impact on seismic hazard assessments remains unclear. Understanding how seismic and aseismic slip interact is crucial and requires characterizing the slip of SSEs and their relationships with interseismic coupling and seismic activity (Radiguet *et al.* 2012; Wallace *et al.* 2016; Nishikawa *et al.* 2023; Jara *et al.* 2024). Several authors have highlighted the relevance of the SSEs for seismic hazard (Dixon *et al.* 2014; Obara & Kato 2016; Uchida *et al.* 2016; Voss *et al.* 2018; Cruz-Atienza *et al.* 2021; Saux *et al.* 2022; Nishikawa *et al.* 2023). However, quantifying the impact of this information on seismic hazard assessments has not yet been explored.

In this study, we first review SSEs in Costa Rica (Table A1), where some of the largest shallow and deep SSEs have been well-documented in the last 20 yr (Outerbridge *et al.* 2010; Jiang *et al.* 2012, 2017; Dixon *et al.* 2014; Voss *et al.* 2017; Xie *et al.* 2020; Perry *et al.* 2023; Dascher-Cousineau & Bürgmann 2024). Furthermore, we assess the impact of incorporating SSEs and geodetic information for the subduction zone of Costa Rica in probabilistic seismic hazard assessment (PSHA).

Costa Rica is a seismically active country in Central America, with a history of at least 68 damaging earthquakes since 1821 (Linkimer *et al.* 2018). This high seismicity mainly originates from the subduction of the Cocos plate underneath the Caribbean plate and the Panama microplate. The Cocos plate subducts beneath the Middle American Trench at a rate of approximately 83–89 mm yr<sup>-1</sup> (DeMets *et al.* 2010), with a volcanic arc situated ~150 km to the northeast of the trench (Fig. 1). The Panama triple junction marks the end of this trench to the southeast, where it meets the Panama Fracture Zone (PFZ), a right-lateral strike-slip fault separating the Cocos and Nazca plates (Fig. 1). Moving eastwards, the boundary between the Panama and Nazca plates is the Southern Panama Deformed Belt (SPDB), identified as an oblique subduction zone in western Panama (Kolarsky & Mann 1995; Westbrook *et al.* 1995). The northern and western boundaries between the Caribbean plate and the Panama microplate are broad zones of crustal deformation. The Central Costa Rica Deformed Belt (CCRDB) consists mainly of

strike-slip faults, while the North Panama Deformed Belt (NPDB) comprises a series of submarine thrusts and folds (Adamek *et al.* 1988; Fan *et al.* 1993; Marshall *et al.* 2000; Montero 2001). Additionally, strike-slip faults run along the volcanic arc in Nicaragua and northern Costa Rica (VAF), facilitating northwestward movement of the Central America forearc block (CAFAB; LaFemina *et al.* 2009; Kobayashi *et al.* 2014).

Previous probabilistic seismic hazard assessments (PSHAs) for Costa Rica have been progressively more detailed, in order to account for such a complex tectonic setting (Mortgat *et al.* 1977; Rojas *et al.* 1993; Benito *et al.* 2012; Global Earthquake Model (GEM) 2018, 2023; Calderon & Silva 2019). Recently, Hidalgo-Leiva *et al.* (2023) published the 2022 Seismic Hazard Model for Costa Rica (CRSHM 2022). This model incorporates updates on Costa Rican seismotectonics, the selection of the most suitable ground motion models (GMM) and improved the characterization of seismic sources. However, neither this nor any of the previous PSHA models integrated geodetic information or SSEs into the magnitude–frequency distribution (MFD) of seismic sources. Therefore, incorporating geodetic data and SSEs may better assess the effect of aseismic processes on seismic hazard, neglected when only the seismic catalog is considered.

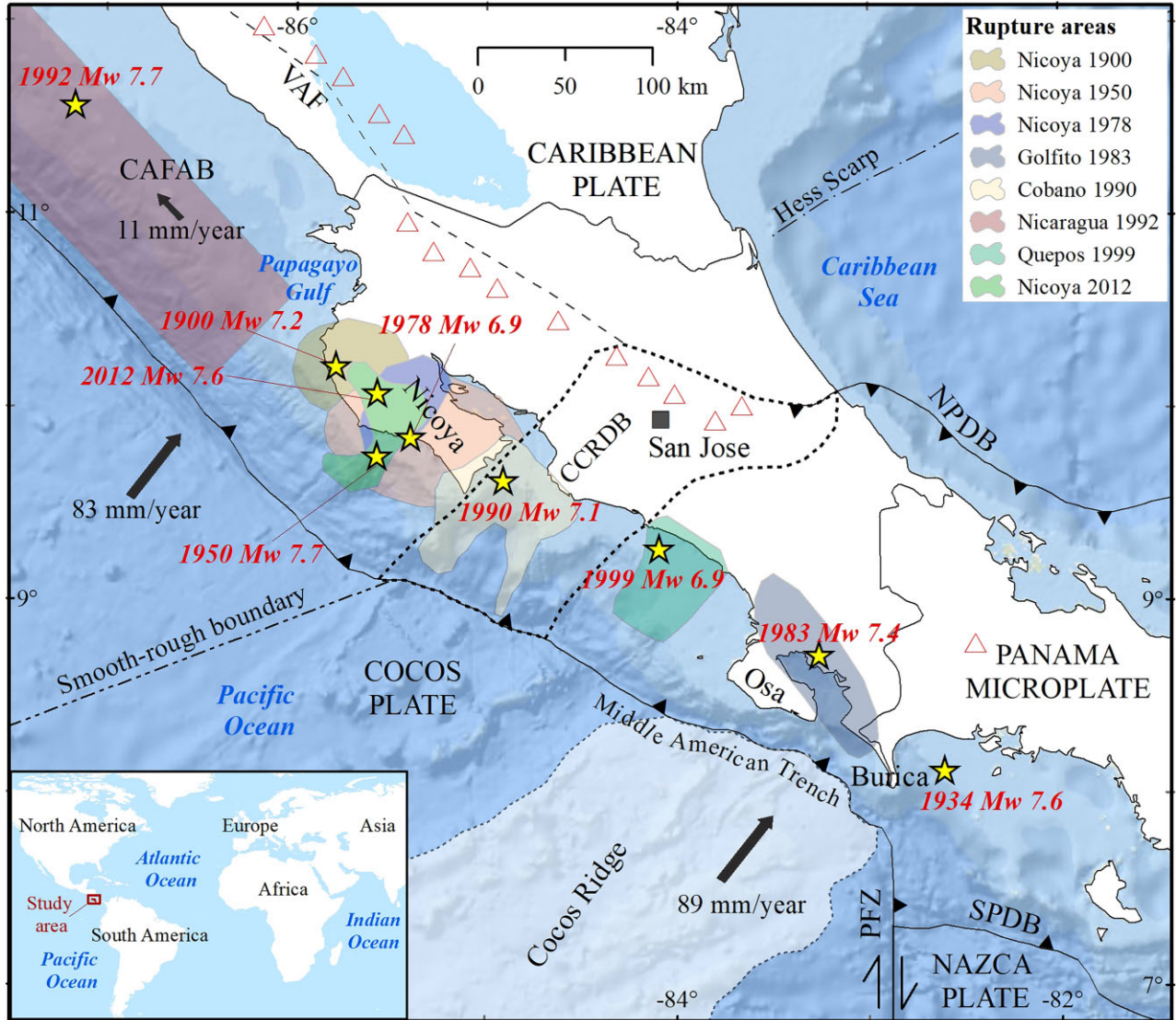
Incorporating SSEs and geodetic information in PSHA may be addressed from two different perspectives: (1) in terms of triggering or inhibiting earthquakes due to stress changes (forecast and time-dependent seismic hazard) and/or (2) in terms of long-term seismic moment budget, based on seismic slip rates, to approach seismic recurrence parameters used in PSHA. Here, we focus on the second one, accounting for the seismic moment budget based on a complementary use of geodetic information from SSEs, and the CRSHM 2022, which used seismic catalogue information.

The MFD is typically defined by the Gutenberg & Richter (1944) law, relying solely on seismic catalogues. Globally, only a few studies have incorporated geodetic data to better constrain the seismic potential, either by estimating earthquake rates above a minimum magnitude ( $N_{\min}$ ) or assessing maximum magnitudes ( $M_{\max}$ ) on the subduction interface (Stirling *et al.* 2012; Avouac 2015; Bird *et al.* 2015; Kagan & Jackson 2016; Rollins & Avouac 2019; Bayona *et al.* 2021; Michel *et al.* 2021, 2023). In this context, integrating geodetic observations complement seismic catalogues, refine the characterization of magnitude–frequency distribution and yield more robust seismic hazard assessments.

We present a compilation of SSEs in Costa Rica based on an in-depth review of previous studies, exploring viable ways to incorporate them in seismic hazard assessments. We also evaluate the influence of SSEs on the seismic moment release, the impact of the subduction segmentation in PSHA computations, and explore ways to fully integrate geodetic data and earthquake catalogues. Finally, we compare our results with the CRSHM 2022 and explore epistemic uncertainties within this new framework, highlighting the relevance of including geodetic information in PSHA. To facilitate readability, Table 1 lists main acronyms and key terms most used throughout the text.

## 2 SLOW-SLIP EVENTS (SSEs) IN COSTA RICA

In Costa Rica, interplate earthquakes of  $M_w \geq 7.0$  occur approximately every 30–40 yr (Montero 1986), with the 2012  $M_w$  7.6 Nicoya earthquake being the most recent (Protti *et al.* 2014)



Downloaded from https://academic.oup.com/gji/article/242/2/gjaf204/8156706 by guest on 26 June 2025

**Figure 1.** Costa Rican seismotectonic context. The region contained within the dotted lines represents the Central Costa Rica Deformed Belt (CCRDB). The dashed line represents the simplified northeast boundary of the Central America forearc block (CAFAB) along the volcanic arc faults (VAF). NPDB: North Panama deformed belt; PFZ: Panama fracture zone; and SPDB: South Panama deformed belt. Stars are the epicentres of the main subduction interplate earthquakes (Linkimer *et al.* 2018) and shaded areas represent the rupture area of those events (Feng *et al.* 2012; Protti *et al.* 2014); triangles are active volcanoes, and the square is the capital city of San Jose.

(Fig. 1). Here, the Nicoya and Osa peninsulas are very close to the trench, directly above the seismogenic zone, providing an excellent opportunity to accurately capture shallow SSEs. This section outlines SSEs along the Costa Rican subduction margin (Fig. 2) (Xie *et al.* 2020; Baba *et al.* 2021; Perry *et al.* 2023), which occur alongside large regular and tsunami earthquakes (Feng *et al.* 2012).

In the Nicoya peninsula, geodetic monitoring began in 2002 with the first onshore continuous Global Navigation Satellite System (GNSS) station, expanding since then with up to 33 GNSS stations by 2020, most of them managed by the Observatorio Sismológico y Vulcanológico de Costa Rica (OVSICORI-UNA; Jiang *et al.* 2012, 2017; Xie *et al.* 2020; Baba *et al.* 2021). Additionally, offshore seafloor pressure recorders (Davis & Villinger 2006), and broadband and short-period seismometers have been operating, and their densification has increased since 2007 (Jiang *et al.* 2017). In the Nicoya peninsula, shallow and deep SSEs occur, and most studies

agree that the first well-detected one occurred in 2003 (Davis & Villinger 2006). However, it has also been suggested that an earlier SSE occurred in 2000 (Gao *et al.* 2012). Here, for an SSE detection threshold of  $M_w$  6.5, a recurrence interval of about two years (Fig. 2b) has been identified (Jiang *et al.* 2012; Voss *et al.* 2018; Xie *et al.* 2020). SSEs in Nicoya are correlated to seismic tremors (Outerbridge *et al.* 2010) and generally occur outside the main coseismic rupture zone, often marking its boundaries (Dixon *et al.* 2014; Voss *et al.* 2018).

Perry *et al.* (2023) first characterized SSEs in the Osa Peninsula using observations from stations established in 2010, expanded in 2016–2018, and supplemented in 2022, mainly by OVSICORI-UNA. With a detection threshold of  $M_w$  6.5, they identified two SSEs in 2018 and two more in 2022 (Fig. 2c) and suggested an additional event in 2013, detected by the lone station at the time (RIOS). These observations indicate a recurrence interval of about four years. Based on the spatial distribution of these SSEs, another

**Table 1.** Main and most used acronyms in this paper.

Acronym	Explanation
CRSHM 2022	2022 Seismic Hazard Model for Costa Rica
Csi11	Nicoya Peninsula interplate source
Csi12	Central Pacific interplate source
Csi13	Osa Peninsula interplate source
$C_v$	Coefficient of variation of the series of large earthquakes
GMM	Ground motion model
GNSS	Global Navigation Satellite System
GR	Gutenberg–Richter
MFD	Magnitude–frequency distribution
$M_{\max}$	Maximum magnitude
$M_{\min}$	Minimum magnitude threshold
$M_0$	Seismic moment
$M_{0,\text{Char}}$	Seismic moment of the characteristic earthquake
$\dot{M}_0$	Moment rate
$M_w$	Moment magnitude
$N_{\min}$	Earthquake rates from a minimum magnitude threshold
PGA-475yr	Peak ground acceleration at return periods of 475 yr
PSHA	Probabilistic Seismic Hazard Analysis
$R_p$	Recurrence period of large earthquakes
SSE	Slow-slip event
$T_r$	Return period
$X$	Seismic coupling coefficient (Zöller 2024)
$\alpha$	Fraction of transient slip that is seismic (Avouac 2015)
$\mu$	Shear modulus
$\dot{s}$	Seismic slip rate

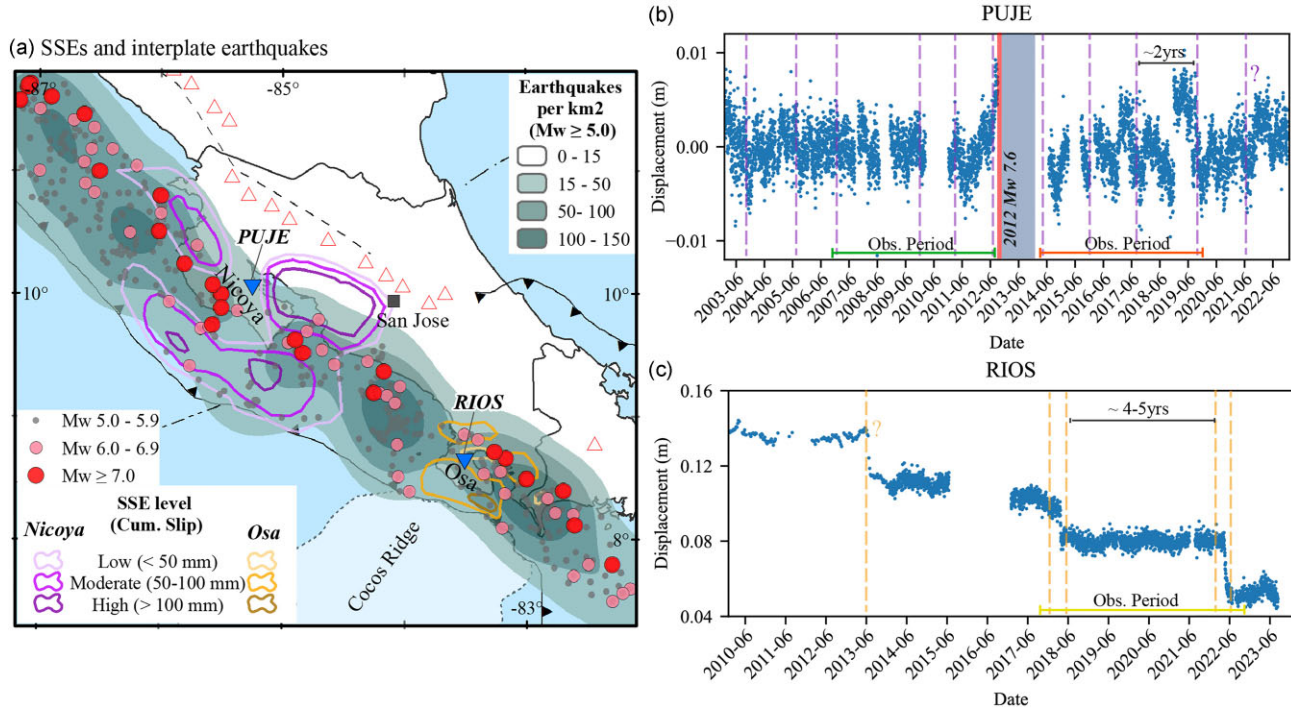


**Figure 2. SSEs in Costa Rica.** (a) SSEs and interplate earthquakes. Detrended GNSS north component of PUJE station in Nicoya peninsula (b) and RIOS station in Osa Peninsula (c). For both stations seasonal and coseismic effects from minor earthquakes are not removed. Dashed vertical lines in panels (b) and (c) indicate SSEs reported in Xie et al. (2020) and Perry et al. (2023), respectively, while the solid vertical line in panel (b) indicates the 2012  $M_w$  7.6 Nicoya earthquake and shaded area its post-seismic deformation. The horizontal line represents the average recurrence periods of SSEs, and coloured horizontal lines indicate observational periods considered for the seismic slip rate approach. Seismic catalogue (a) is from the National Seismological Network of Costa Rica, and Arroyo-Solórzano and Linkimer (2021).

**Table 2.** SSEs observations relevant for seismic hazard in Costa Rica.

Main features	Yes/No/Other	Comments/Seismic hazard implications
SSE magnitudes	$M_w$ 6.5–7.2	Seismic moment released aseismically.
Foreshocks and SSE migration	Yes	Observed in Nicoya, before the 2012 $M_w$ 7.6.
Shallow SSEs	Yes	In Nicoya and Osa. Suggested as limits of the size of future earthquakes.
Deep SSEs	Yes	The most important recurrent patch is located in the Nicoya gulf.
Swarms and repeaters	Yes	In Nicoya it is very common. In Osa not well defined yet, but probably.
SSE and regular earthquakes	Usually not	In Nicoya the patch of the largest recurrent earthquakes is outside SSE regions.
Coupling in SSE region	Intermediate	During inter-SSEs periods, these regions can present intermediate or even high coupling.
Changes in Coulomb stress	Not enough	In Nicoya the changes prior to the 2012 $M_w$ 7.6 earthquake were not enough to correlate with the SSEs occurrence.
b-value in SSE region	0.69–1.10	0.83 is the general b-value for interplate earthquakes in CR. In the Nicoya segment is 0.69, in Central Pacific 1.10 and in Osa 0.84.
Seamount's presence	Yes	In Central and Southern Pacific of Costa Rica. Relevant for SSE in Osa and for the patch in the Nicoya gulf.
SSE role in seismic rupture	Yes	Aseismic release of elastic energy and barriers for large earthquake generation and for tsunamigenic potential in Nicoya and Osa.
Kinds of interaction	Not clear	Not well defined yet if there is a clear relationship between SSEs and large earthquakes.
SSE recurrence period	2–4 yr	In Nicoya defined as 2 yr and in Osa 4 yr (for $M_w > 6.5$ ).

key inference from Perry *et al.* (2023) is that a future large earthquake is less likely to rupture the up-dip region of maximum slow slip, potentially limiting its size.

This background allows us to summarize relevant features of SSEs related to seismic hazard in Costa Rica (Table 2). First, the SSEs activity in both peninsulas is accommodating part of the interplate deformation budget, aseismically releasing elastic energy, which cannot be released by regular earthquakes. This activity, and the recurrent shallow and deep SSEs occurring there (Fig. 2a), could potentially limit the size of future earthquakes and their tsunamigenic potential (Dixon *et al.* 2014; Jiang *et al.* 2017; Perry *et al.* 2023). Second, usually, SSE regions do not overlap with large, regular earthquake ruptures (Figs 1 and 2a). However, at times, part of the rupture may propagate along the SSE patch, with the same patches exhibiting intermediate to high coupling when no SSEs occur (Voss *et al.* 2018; Xie *et al.* 2020).

Another key parameter is the *b*-value in the Gutenberg & Richter (1944) law which describes the relative abundance of large versus small earthquakes. This parameter is also considered a stress proxy, being inversely proportional to differential stress (Scholz 2015; Matsumoto *et al.* 2024). In the Costa Rican subduction zone, the *b*-value characterization reveals an increasing stress trend (decreasing *b*-value) from the Central Pacific toward Nicoya and Osa (Arroyo-Solórzano & Linkimer 2021). The highest *b*-value in the Central Pacific correlate well with the presence of subducted seamounts and, to some extent, with the subduction of the Cocos Ridge in the Southern Pacific. In subduction zones, subducted seamounts and ridges have also been correlated to high *b*-values (Ghosh *et al.* 2008a; Legrand *et al.* 2012; Zhou & Xia 2020). The surrounding region of a subducting seamount may be aseismically sliding (correlating with high *b*-values) while the seamount acts as a strong asperity which prevents aseismic sliding and only breaks in occasional large earthquakes (Lee *et al.* 2023). Also, seamounts may be constituted by hydrothermally altered rocks, which could dehydrate when subducted, increasing the pore pressure and reducing the effective shear stress, so high *b*-values could also be indicative of slab dehydration (Legrand *et al.* 2012).

Finally, in terms of earthquake triggering, foreshocks and SSE migration were reported prior to the 2012  $M_w$  7.6 Nicoya earthquake. Nevertheless, changes in Coulomb stress before the event were insufficient to confirm a direct effect on the trigger of the earthquake (Voss *et al.* 2018). In conclusion, we can state that the

interaction between SSE and major earthquakes remains unclear, but its definition and characterization may be useful for seismic hazard approaches, as we present in the following sections.

### 3 SEISMIC SOURCE MAGNITUDE-FREQUENCY DISTRIBUTION (MFD)

#### 3.1. Seismic slip rate approach

We estimate the seismic slip rate based on the long-term slip deficit definition, using SSE observations in Costa Rica (Fig. 3a and Table undefinedA1). The cumulative slip from SSEs is calculated over distinct 6-yr observation periods (two for Nicoya and one for Osa, Figs 2b and c). For Nicoya, the periods were defined according to the slip reported by Xie *et al.* (2020): (1) 2007–2012 and (2) 2014–2019, excluding the post-seismic deformation from the 2012  $M_w$  7.6 Nicoya earthquake. Similar cumulative slip estimates for both periods support their representativeness for the long-term slip deficit in Nicoya. For Osa, we use the 2018–2023 period, being this the only robust cumulative SSE slip estimation available for this region (Perry *et al.* 2023).

We consider both segmentation and non-segmentation along the subduction interface. For segmentation, we use the regional seismogenic zoning for Central America from Alvarado *et al.* (2017), and the geometries refined for Costa Rica in Hidalgo-Leiva *et al.* (2023). In their nomenclature for interplate sources, each abbreviation starts with the letter C for Costa Rica, followed by a 'si' and a number. Sources analysed in detail here are the Nicoya Peninsula (Csi11), the Central Pacific (Csi12), and the Osa peninsula (Csi13). This segmentation (Figs 3b and c) is based on previous studies identifying key variations along the Costa Rica interface, such as earthquake occurrences, dip angles, seamounts, bathymetric features and recurrence intervals (Montero 1986; Montero *et al.* 1992; Protti *et al.* 1994).

We use as initial input the convergence rates from the PVEL model (DeMets *et al.* 2010) and discount the aseismic slip due to SSEs to estimate seismic slip rates along the interface. Namely, we assume that non-SSE areas in the seismogenic zone (10–40 km) are fully locked, accumulating the convergence rate during the observation period, while SSE areas release part of the slip aseismically,

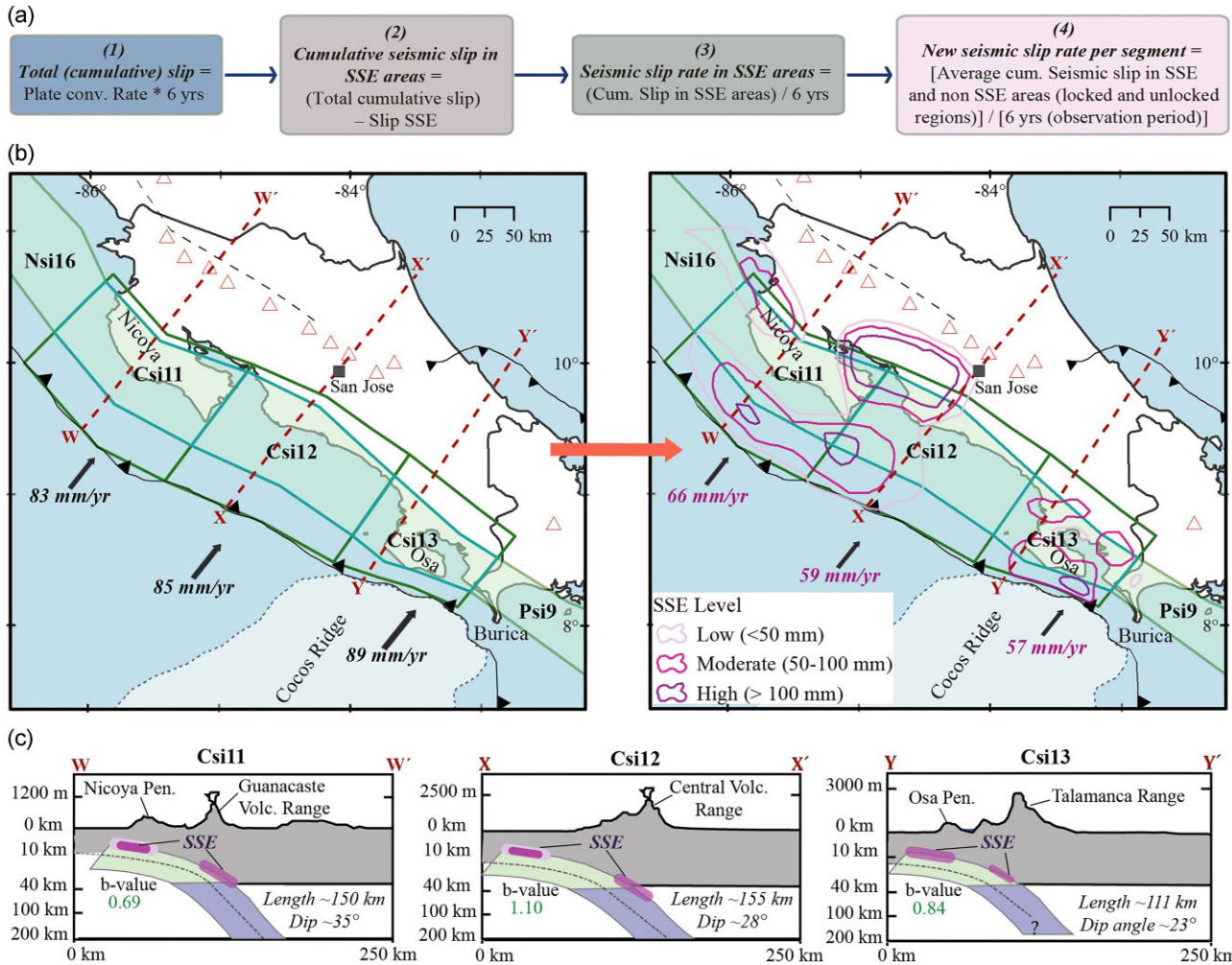


**Figure 3. Seismic slip rate approach.** (a) Flow diagram for the definition of the long-term slip deficit from SSEs for the seismic slip rates estimation, based on the convergence rates from the PVEL model (DeMets *et al.* 2010). (b) Subduction interface segments from Alvarado *et al.* (2017) and seismic slip rate discounted for the seismic moment budget estimation. The left panel shows the total convergence rate, and the right panel, the seismic slip rate. Dashed lines represent cross sections in panel (c). (c) Cross-sections of the subduction segments in Costa Rica indicating their length and dip angles of subduction segments.

resulting in lower long-term seismic slip rates. Additionally, we assume the long-term slip rate on the interface equals the horizontal convergence rate across the plate boundary, with no anelastic deformation in either plate (Avouac 2015). Although initially simplistic, these assumptions allow for a comprehensive segment characterization, which is essential for the seismic hazard source model. Using this slip deficit, we estimate seismic slip rates per subduction segment and compute a weighted average value, based on the area of SSEs level patches on each segment, yielding a single seismic slip rate per segment (Fig. 3b).

### 3.2. MFD from moment budget

We start by assuming that magnitudes of earthquakes generated by the seismic sources follow a functional form of the exponential Gutenberg–Richter (GR) relation (Gutenberg & Richter 1944), which is a power law distribution of seismic moment, up to  $M_{\max}$ . Based on this assumption, we evaluate the seismic potential according to the moment rate budget ( $\dot{M}_0$ ) resulting from considering SSEs (Fig. 4):

$$\dot{M}_0 = \dot{s} \cdot \mu \cdot A, \quad (1)$$

where  $\dot{s}$  is the seismic slip rate,  $\mu$  is the shear modulus and  $A$  is the seismogenic area (Brune 1968).

We use the  $\dot{s}$  obtained in Section 3.1, a shear modulus of  $\mu = 30$  GPa (Hanks & Kanamori 1979) and the interface rupture plane area of each segment according to its geometry characterization from Hidalgo-Leiva *et al.* (2023). We assess this result using the MFD of the sources, considering variations in (1)  $N_{\min}$  from seismic slip rates and (2)  $M_{\max}$  from the moment budget closure condition (Figs 4a and b). Moreover, we explore three different options of geometries and  $b$ -values (Fig. 4c). This results in six combinations (1a, 1b, 1c, 2a, 2b, 2c), for which we explore the influence of incorporating SSEs. These labels are used hereafter to refer to each scenario, considering SSEs or not. Finally, we weigh these alternatives to account for epistemic uncertainties from methods, geometries and size–magnitude relations. The main assumptions are:

- (i) CRSHM 2022 is taken as reference for comparisons and for the use of seismic parameters ( $M_{\max}$ ,  $N_{\min}$  and  $b$ -values), and all seismogenic zones follow a G-R MFD.
- (ii) The interseismic slip deficit by observation period (6 yr) can be extrapolated to longer timescales.

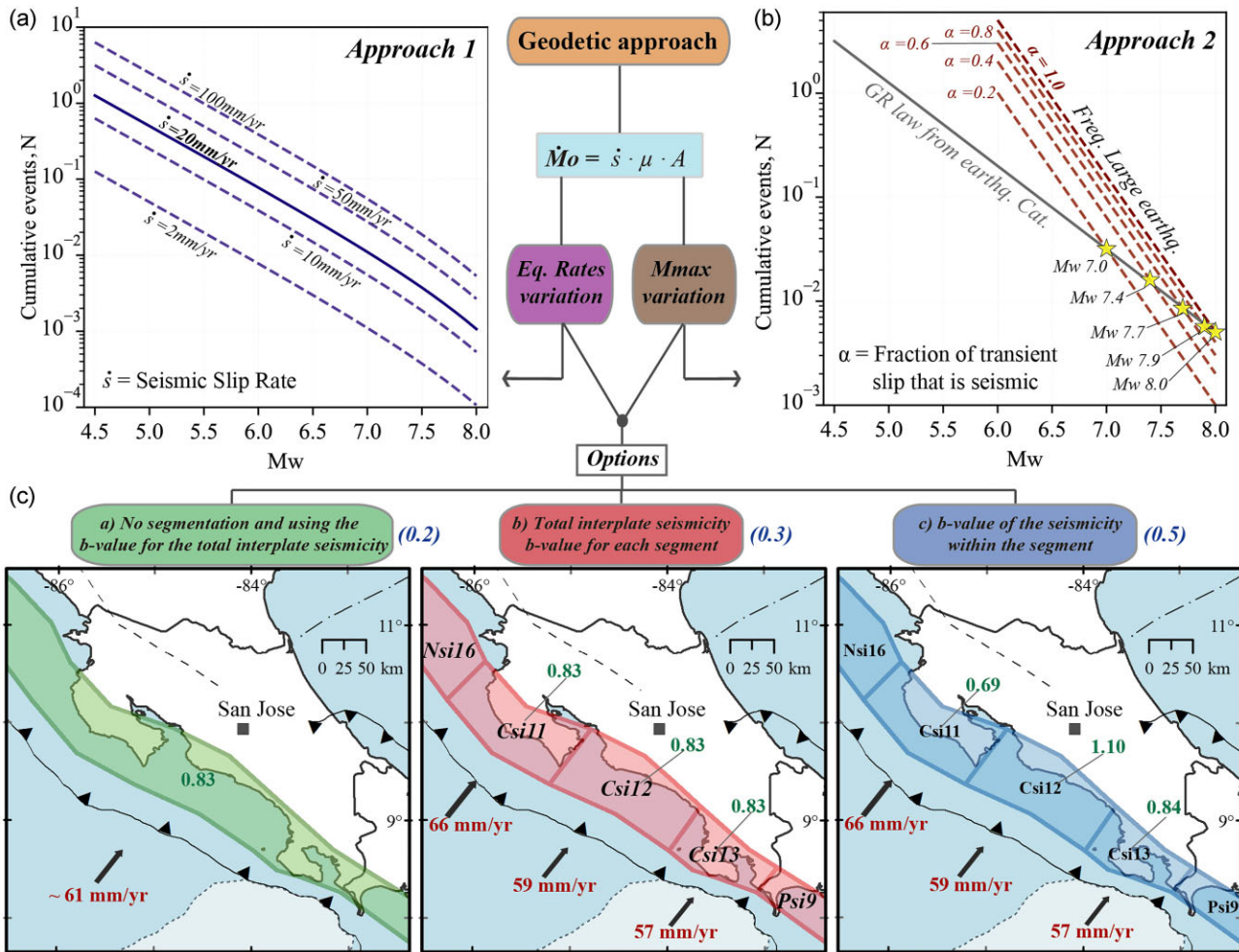


**Figure 4.** Approaches for the MFD characterization. (a) Example fixing  $M_{\max}$  to  $M_w$  8.0 for a fault with a length of 120 km, aspect ratio of 2, shear modulus of  $\mu = 30$  GPa,  $b$ -value of 0.8 and a seismic slip rate of  $20 \text{ mm yr}^{-1}$ . Dashed lines represent variations from the original slip rate (thick line). (b) Example fixing earthquake rates for the same fault varying the seismic/aseismic factor ( $\alpha$ ). Dashed lines show the frequency of large earthquakes when their magnitudes are varied for different values of  $\alpha$ . Stars at the intersection of the lines indicate the  $M_{\max}$  inferred by this approach from the slip budget closure. (c) Options of geometries and  $b$ -values assumed, and the corresponding seismic slip rates. Values in parentheses represent the weight for each option in the logic tree used for hazard calculations.

(iii) The long-term slip rate on the interface is equal to the horizontal convergence rate across the plate boundary, with neither plate experiencing anelastic internal deformation.

(iv) SSE patches are represented by the average seismic slip rate per segment, while locked areas (without SSEs) are assumed to be fully coupled in the long term.

(v) The historical catalogue (1520–2020) is complete and representative for earthquakes  $M_w > 7.0$ .

### 3.2.1. From moment rates to earthquake rates - $N_{\min}$ - (approach 1)

For this approach, we consider magnitudes from  $M_w \geq 4.5$  up to a fixed  $M_{\max}$ , given by the CRSHM 2022. The earthquake rate ( $N_{\min}$ ) for this magnitude threshold ( $M_{\min}$ ), represents the average annual seismic moment accumulated in each segment that will be released by earthquakes from  $M_{\min}$  to  $M_{\max}$  (Fig. 4a). Several widely used models relate slip rates to  $N_{\min}$  (Table 3) following either a truncated or tapered GR distribution with nearly identical parameters (Molnar 1979; Anderson & Luco 1983; Youngs & Coppersmith 1985; Bungum 2007; Rivas-Medina *et al.* 2018).

Our first two models are based on Anderson & Luco (1983), who proposed three functional forms to constrain earthquake occurrence based on slip rates. These functional forms relate parameters such as the seismic moment scaling coefficient,  $b$ -value, fault area, shear modulus, slip-length ratio ( $1.25 \cdot 10^{-5}$  for plate margins (Scholz 1982)), seismic moment and  $M_{\max}$  (Table 3). The key difference between these models is that the functional form 1 uses a truncated exponential function, while functional forms 2 and 3 combine the exponential function with a constant, causing the rate to approach zero at  $M_{\max}$ . We use the functional form 1 as our model 1 and the average of functional forms 2 and 3 (rather similar) as our model 2. As a result, our model 2 shows a smooth transition towards  $M_{\max}$ . Then, for our model 3 we adopt the approach from Youngs & Coppersmith (1985), who proposed an exponential MFD constrained by the upper bound magnitude ( $M_{\max}$ ),  $b$ -value and moment rate (Table 3). Lastly, our model 4 uses the equation from Molnar (1979), which applies the GR relation and seismic moment to estimate the relative recurrence of events based on an empirical relation between magnitude and seismic moment (Table 3). We implement all those alternatives and obtain the average  $N_{\min}$  by source for its use in seismic hazard computations.

**Table 3.** Models and their dependences used for MFD characterization of the source from geodetic data.

Models	Variables and its dependences
<b>Earthquake Rates (<math>N_{\min}</math>) variation</b>	
<b>Model 1:</b> Equation I.10 in Anderson & Luco (1983)	$b = b$ -value, of the GR relationship (from the CRSHM 2022**).
$N_{\min} = \left(\frac{d-\beta}{d}\right) \cdot \left(\frac{\dot{s}}{\gamma}\right) \cdot e^{\beta(M_{\max}-M_{\min})} \cdot e^{-\left(\left(\frac{d}{2}\right) \cdot M_{\max}\right)}$	$d = 1.5 \cdot \ln(10)$
<b>Model 2*:</b> Equation II.9 in Anderson & Luco (1983)	$\beta = b \cdot \ln(10)$
$N_{\min} = \left(\frac{d-\beta}{\beta}\right) \cdot \left(\frac{\dot{s}}{\gamma}\right) \cdot [e^{\beta(M_{\max}-M_{\min})} - 1] \cdot e^{-\left(\left(\frac{d}{2}\right) \cdot M_{\max}\right)}$	$\dot{s}$ = Slip rate, depending on considering or not SSEs (seismic slip rate). $\gamma = \sqrt{(\sigma \cdot M_{\text{Mo}})/(\mu \cdot W)}$ , where $\sigma$ is the slip/length ratio; $M_{\text{Mo}}$ is the seismic moment for $M = 0$ ; $\mu$ is the shear modulus and $W$ is the seismogenic width.
And equation III.9 in Anderson & Luco (1983)	$M_{\max}$ is the maximum magnitude (from the CRSHM 2022).
$N_{\min} = \frac{d \cdot (d-\beta)}{\beta} \cdot \left(\frac{\dot{s}}{\gamma}\right) \cdot \left\{ \frac{1}{\beta} [e^{\beta(M_{\max}-M_{\min})} - 1] - (M_{\max} - M_{\min}) \right\} \cdot e^{-\left(\left(\frac{d}{2}\right) \cdot M_{\max}\right)}$	$M_{\min}$ is the minimum magnitude threshold defined ( $M_w$ 4.5). $\dot{M}_0$ is the moment rate of the subduction segment, given as $\dot{M}_0 = \dot{s} \cdot \mu \cdot A$ , where $\dot{s}$ is the slip rate, $\mu$ the shear modulus, and $A$ is the seismogenic area.
<b>Model 3:</b> Youngs & Coppersmith (1985)	$M_{\text{Mo}}$ is the seismic moment of the $M_{\max}$ associated.
$N_{\min} = \frac{M_0 \cdot (d-b)}{b \cdot M_{\text{Mo}} \cdot M_{\max}} \cdot [1 - e^{-\beta(M_{\max}-M_{\min})}]$	$M_{\text{Mo}}$ is the seismic moment of the $M_{\min}$ defined.
<b>Model 4:</b> Molnar (1979)	
$N_{\min} = \left(1 - \frac{2b}{3}\right) \cdot \frac{\dot{M}_0}{M_{\text{Mo}} M_{\max}} \cdot \left(\frac{M_{\text{Mo}} M_{\max}}{M_{\text{Mo}} M_{\min}}\right)^{\frac{2b}{3}}$	$\alpha = \chi s / (\chi s + \chi a s + \chi SSE)$ , where $\chi s$ is the seismic coupling (ratio of cumulative seismic slip to long-term slip), $\chi a s$ aseismic coupling due to afterslip and $\chi SSE$ is the aseismic coupling due to SSE (ratio of cumulative aseismic SSEs to long-term slip).
<b><math>M_{\max}</math> variation</b>	
$\log N = \frac{-3}{2} \cdot M_w - \log \dot{M}_0 + \log [\alpha \cdot (1 - \frac{2b}{3})]$	
From Avouac (2015), based on Molnar (1979), but accounting for aseismic processes.	

\* We used the average of both equations presented due to their similarity. \*\*CRSHM 2022: The 2022 Costa Rica Seismic Hazard Model (Hidalgo-Leiva *et al.* 2023).

### 3.2.2. From moment rates to maximum magnitudes - $M_{\max}$ - (approach 2)

In the  $M_{\max}$  evaluation fixing earthquake rates, we explore possible values of  $M_{\max}$  that fulfil the slip budget closure condition (Fig. 4b; Avouac 2015; Rollins & Avouac 2019; Michel *et al.* 2023). This analysis constrains the GR relationship obtained from the seismic catalogue with a new curve that incorporates the seismic slip fraction ( $\alpha$ ) into the Molnar (1979) model (Table 3). The new curve is compared with the GR from the catalogue (CRSHM 2022) to determine the  $M_{\max}$  that balances the slip budget. This  $M_{\max}$  is crucial, as seismic moment increases significantly with magnitude, being a key parameter in hazard assessments.

### 3.2.3. Geometry and $b$ -value assumptions

To show the effects of different assumptions considered, we determine the MFD based on the recurrence parameters of the GR for each branch of the logic tree in the seismic source model. For earthquake rate variations (approach 1), the results show different values from CRSHM 2022 in  $a$ -values and  $N_{\min}$  (Figs 5a, 6a, c and e; see also Figs B1 and B2 in appendices for the full visualization of the models used). The  $M_{\max}$  variation (approach 2) also differs from CRSHM 2022, but in terms of  $M_{\max}$  (Figs 5b, 6b, d and f), based on the magnitude needed to close the seismic moment budget in the seismogenic zone (Avouac 2015; Rollins & Avouac 2019; Michel *et al.* 2023). Table B1 summarizes the source model characterization, with or without SSEs, for both approaches ( $N_{\min}$  and  $M_{\max}$  variations) across three source geometry options under different  $b$ -value assumptions: (a) no segmentation, (b) segmentation using the  $b$ -value for the total interplate seismicity and (c) segmentation using the  $b$ -value based on each segment's seismicity.

**3.2.3.1. No interface segmentation (option a)** The approach evaluating  $N_{\min}$  without segmentation and considering SSEs (*1a SSEs*) shows lower average earthquake rates compared to CRSHM 2022

(Fig. 5a). With  $M_{\max}$  fixed at  $M_w$  8.1 (Arroyo-Solórzano & Linkimer 2021), the most significant differences occur between  $M_w$  7.0 to 8.1. In contrast, without SSEs (*1a No SSEs*), our geodetic approach yields a higher average  $N_{\min}$  for  $M_w$  4.5–7.5, with values nearly matching between  $M_w$  7.5 and 8.1 (Fig. 5a). This suggests that including SSEs aligns better with intermediate magnitudes in the GR curve from the catalogue and indicates that SSEs may reduce the likelihood of large earthquakes based on the seismic slip rate moment budget.

For the  $M_{\max}$  approach without segmentation and considering SSEs (*2a SSEs*), we use a mean convergence rate of 85 mm yr<sup>-1</sup> along the Costa Rican trench. The average seismic slip rate, considering SSEs in the segments evaluated, is 61 mm yr<sup>-1</sup> (Fig. 4c). The ratio of these values gives ~72 per cent as the fraction of transient slip that is seismic ( $\alpha = 0.72$ ). Using this value within the interseismic coupling model (Avouac 2015), and comparing the resulting MFD with the GR curve for interplate seismicity (Arroyo-Solórzano & Linkimer 2021),  $M_{\max}$  is constrained at  $M_w$  8.4 (Fig. 5b). This result suggests an increase of 0.7 magnitude units from the observed  $M_{\max}$  ( $M_w$  7.7) in the 1950 Nicoya and 1992 Nicaragua earthquakes (Güendel 1986; Kanamori & Kikuchi 1993) and 0.3 units from the inferred  $M_{\max}$  in CRSHM 2022 ( $M_w$  8.1). Additionally, assuming no aseismic processes ( $\alpha = 1$ ) results in an  $M_{\max}$  of  $M_w$  8.6 (Fig. 5b), nearly a full magnitude unit higher than observed.

**3.2.3.2. Interface segmentation (options b and c)** We repeated the analysis but considering interface segmentation and using the  $b$ -value from either the total interplate seismicity or the segment-specific seismicity (options b and c in Fig. 4c, respectively). In both cases, with SSEs or not, the resulting relationships with the GR curves from CRSHM 2022 are similar, with higher  $N_{\min}$  or  $M_{\max}$  when SSEs are excluded. Results per segment are presented for both scenarios (Fig. 6).

For  $N_{\min}$  evaluation (*1b* and *1c*), results vary by segments. In Nicoya, both approaches yield lower earthquake rates for  $M_w \geq 6.5$

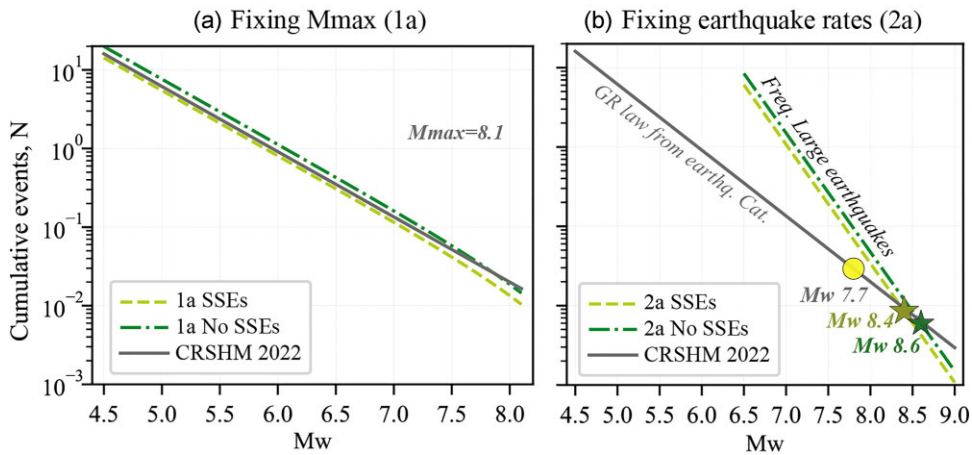


**Figure 5.** Magnitude–frequency distribution without segmentation (option *a* in Fig. 4c) considering SSEs or not. (a) Earthquake rates fixing  $M_{\text{max}}$  to  $M_{\text{w}} = 8.1$ . (b)  $M_{\text{max}}$  fixing earthquake rates. Dashed lines in panel (a) indicate the MFD based on seismic slip rates, while in (b) they represent the frequency of large earthquakes with and without SSEs. The dot in panel (b) represents the  $M_{\text{max}}$  observed while the stars indicate the  $M_{\text{max}}$  inferred from the slip budget closure.

compared to CRSHM 2022. However, assessment *1b* presents higher rates for  $M_{\text{w}}$  range 4.5–6.5, while *1c* practically coincides with the CRSHM 2022 without SSEs and shows slightly lower rates when SSEs are included (Fig. 6a). In contrast, in the Central Pacific and Osa the geodetic approach consistently exceeds the GR curve from the catalogue (Figs 6c and e), indicating that the moment budget is not fully released by the seismicity. In the Central Pacific, the variation in the geodetic curves (*1b* and *1c*) is explained due to the difference between the *b*-value from the total interplate seismicity (0.83) and the *b*-value of the segment (1.10). However, they seem to converge for largest magnitudes ( $M_{\text{w}} > 6.5$ ). In Osa, both approaches are almost the same because *b*-values are similar (0.83 and 0.84 for options *1b* and *1c*, respectively), while the rates with SSEs are substantially lower than those without SSEs (Fig. 6e).

In the  $M_{\text{max}}$  assessment (2b and 2c), the  $\alpha$  value varies by segment based on SSE influence (Fig. 3b). In Nicoya, using a convergence rate of 83 mm yr<sup>-1</sup> with a seismic slip rate of 66 mm yr<sup>-1</sup>, we obtain an  $\alpha = 0.79$ , where the GR of the segment reach the MFD of large earthquakes, at  $M_{\text{w}} = 7.8$  (2b SSEs) and  $M_{\text{w}} = 7.9$  (2c SSEs) (Fig. 6b). Without SSEs ( $\alpha = 1.0$ ),  $M_{\text{max}}$  increases to  $M_{\text{w}} = 7.9$  (2b No SSEs) and  $M_{\text{w}} = 8.0$  (2c No SSEs) (Fig. 6b), while when SSEs are included,  $M_{\text{max}}$  is very similar to the observed  $M_{\text{max}}$  (0.1 to 0.2 units larger than the 1950  $M_{\text{w}} = 7.7$  Nicoya earthquake, Gutiéndel 1986), and fit very well with the  $M_{\text{max}}$  inferred in the CRSHM 2022 ( $M_{\text{w}} = 7.9$ ).

In the Central Pacific, using a convergence rate of 85 mm yr<sup>-1</sup> and a seismic slip rate of 59 mm yr<sup>-1</sup> results in an  $\alpha = 0.69$ . In this case, it is particularly striking that in neither assessment (2b and 2c), with or without SSEs, does the MFD for large earthquakes align with the segment's GR curve at a feasible magnitude (Fig. 6d). Instead, it reaches up to  $\sim M_{\text{w}} 9.2$ , which is physically unrealistic for the segment. This result suggests that the seismicity observed in the GR relationship from the earthquake catalog is insufficient to explain the interseismic slip deficit (Avouac 2015). Therefore, we use the mean of the scaling relations for interplate earthquakes proposed by Allen & Hayes (2017) and Thingbaijam *et al.* (2017), constraining  $M_{\text{max}}$  to  $M_{\text{w}} = 7.7$  (Fig. 6d). This value is 0.6 units higher than the observed  $M_{\text{max}}$  ( $M_{\text{w}} = 7.1$ ) in 1990 and 0.3 higher than the  $M_{\text{max}}$  inferred in the CRSHM 2022 ( $M_{\text{w}} = 7.4$ ). Matching both curves at  $M_{\text{w}} = 7.7$  would require either a tenfold increase in seismicity rates or an extremely low  $\alpha$  value ( $\sim 0.15$ ) to close the moment budget.

For Osa, using a convergence rate of 89 mm yr<sup>-1</sup> and a seismic slip rate of 57 mm yr<sup>-1</sup>, results in  $\alpha = 0.64$ . The segment's GR curve meets the MFD of large earthquakes at  $M_{\text{w}} = 7.8$  (2c SSEs),  $M_{\text{w}} = 7.9$  (2b SSEs),  $M_{\text{w}} = 8.0$  (2c No SSEs), and  $M_{\text{w}} = 8.1$  (2b No SSEs) (Fig. 6f). Such values are significantly higher than the largest earthquake observed in this segment, the 1983  $M_{\text{w}} = 7.4$  Golfito earthquake (Adamek *et al.* 1988), and exceed the CRSHM 2022 estimate ( $M_{\text{w}} = 7.6$ ).

#### 4 SEISMIC HAZARD COMPUTATIONS

The CRSHM 2022 (Hidalgo-Leiva *et al.* 2023) applied a PSHA to calculate hazard curves and maps using the classical integration method of Cornell (1968). This model used the most extensive earthquake database for seismic hazard purposes in Costa Rica (1520–2020) and revised recurrence parameters (Arroyo-Solórzano & Linkimer 2021) based on the seismic source zoning defined by Alvarado *et al.* (2017). In addition, the CRSHM 2022 also refined source geometries and fault-type percentages, selecting and weighting GMMs for each tectonic domain based on observed strong-motion data (Moya-Fernández *et al.* 2020) and a careful selection process (Scherbaum *et al.* 2004). We use the CRSHM 2022 as a starting point (Table 4) and perform seismic hazard computations using the *OpenQuake* engine (Pagani *et al.* 2014).

Our analysis focuses on modifications to interplate sources in CRSHM 2022. To account for the impact of SSEs and geodetic information, we modify the recurrence parameters in SSEs regions according to their moment budgets (Pagani *et al.* 2021). Additionally, we explore the possibility of non-segmentation along the interplate, which was not evaluated in CRSHM 2022. As outlined in Section 3, we define two main approaches, each three different options of geometry and *b*-value (Fig. 7).

We calculate peak ground accelerations (PGA) for all combinations and using the logic tree per approach, assigning weights (Fig. 7) assuming that each segment's seismicity better represents seismotectonic conditions and potential future ruptures based on the segmentation. Hazard computations are performed for a return period ( $T_r$ ) of 475 yr (10 per cent probability of exceedance in 50 yr), considering SSEs or not, to quantify its differences by ratio maps and acceleration profiles from the trench towards the continent. Additionally, we compare final hazard computations for the

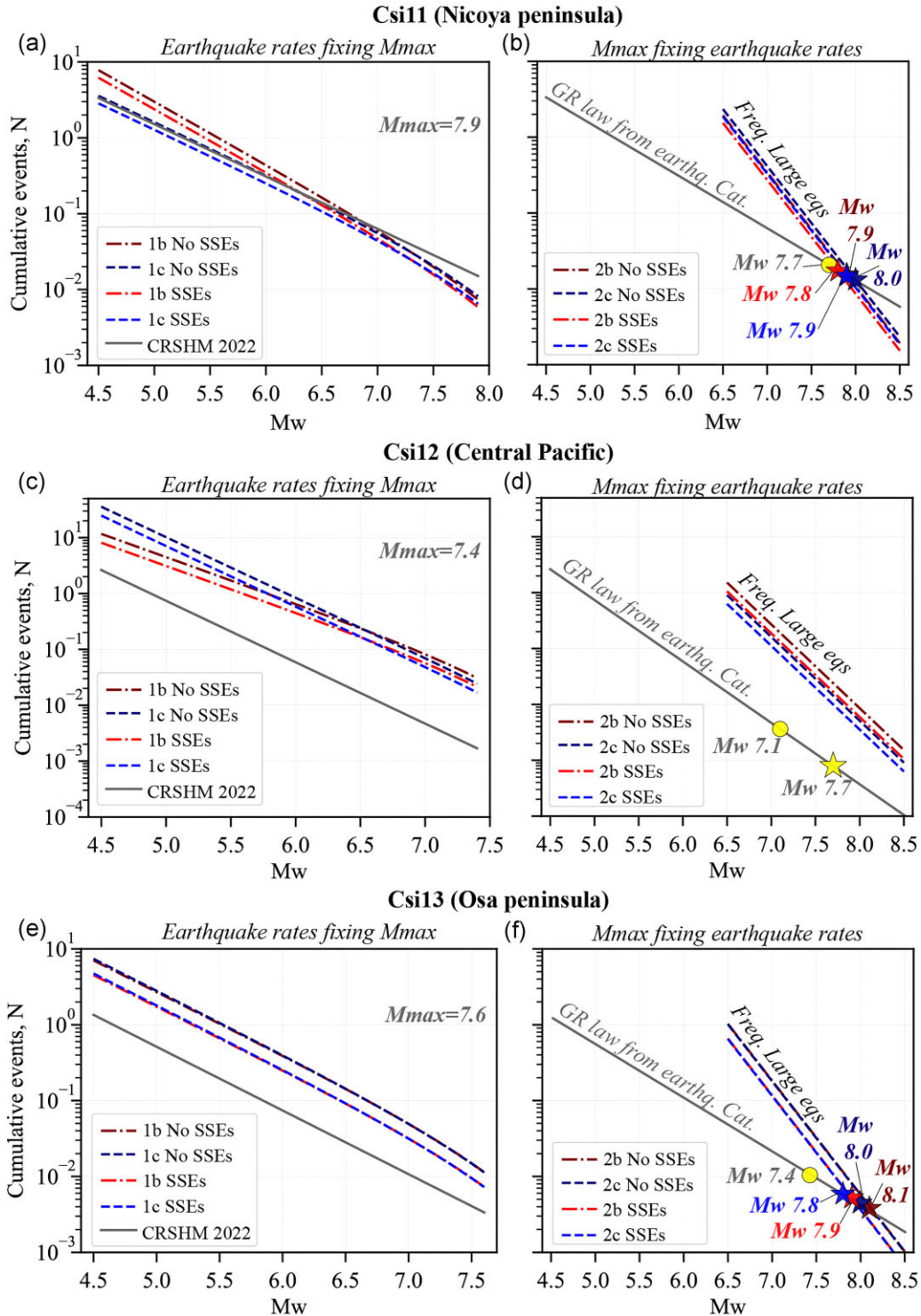


**Figure 6.** Magnitude–frequency distribution using the segmentation (options b and c in Fig. 4c) considering SSEs or not: (1) Earthquake rates fixing  $M_{\max}$ : (a) Csi11, (c) Csi12, (e) Csi13; and (2)  $M_{\max}$  fixing earthquake rates: (b) Csi11, (d) Csi12, (f) Csi13. Dashed lines represent assessments with options (b) and (c). Dots represent the  $M_{\max}$  observed, and stars indicate  $M_{\max}$  inferred from the slip budget closure. In the case of not intersection, the star represents the  $M_{\max}$  inferred from earthquake source scaling relations.

geodetic approach considering SSEs with the CRSHM 2022 by ratio maps and comparing the hazard curves and disaggregation results for some sites of interest (see Figs C1–C4 in appendices for the hazard computations of each branch of the logic tree).

#### 4.1. Considering or not slow-slip events in the geodetic approach

Without SSEs, the  $N_{\min}$  variation yields maximum accelerations up to 1.2 g (Fig. 8a), while including SSEs reduces this to 1.0 g

**Table 4.** Summary of the seismic hazard components of the CRSHM 2022 and its variations for this study.

Seismic hazard components	CRSHM 2022	This study
<b>Seismic source model</b>	Source type and geometry*	Upper-plate sources modelled as ‘area source’. Interplate and intraslab as ‘complex fault’.
	Scaling relations and aspect ratio	Seismic zoning of Alvarado <i>et al.</i> (2017). The seismogenic thickness and top and bottom edges of rupture planes are defined based on a revision of the seismicity and slab geometry contours. The magnitude-scaling used was Wells and Coppersmith (1994) for all the zones. Aspect ratio of 1.5 for all the zones.
	Seismicity parameters*	Taken from Arroyo-Solórzano & Linkimer (2021) based exclusively on the seismic catalog.
	Rupture characterization	-The strike, dip and rake for the most likely rupture plane were defined primarily on recent fault maps and earthquake focal mechanisms.
<b>Ground motion model (GMM)</b>	Logic tree*	No logic tree was used.
	Selection and logic tree	Selected by tectonic domain and intensity measure based on a review of the GMMs available, its contrast with the strong-motion dataset, and its classification and selection based on Scherbaum <i>et al.</i> (2004). Logic trees used by tectonic domain and differentiating weights depending on the intensity measure.
<b>Global parameters</b>	Minimum magnitude, site effect and truncation levels	4.5 $M_w$ , rock conditions with a constant time-averaged shear-wave velocity to a depth of 30 m ( $V_{s30}$ ) of 760 m s <sup>-1</sup> Six truncation levels.
	Intensity measures and return periods	PGA and spectral accelerations (SA) from 0.1 to 3 s and return periods of 475 and 2475 yr.

\* Seismic hazard components in which we introduced changes (highlighted in bold) in this study with respect to the CRSHM 2022.

(Fig. 8b). For the  $M_{\max}$  variation, accelerations decrease from 1.0 g without SSEs (Fig. 9a) to 0.95 g with SSEs (Fig. 9b). Notably, the inclusion of SSEs results in the highest accelerations (>0.55 g) near the trench, particularly in the Nicoya and Osa peninsulas, leading to a more concentrated distribution of high hazard (Figs 8c–e and 9c–e). In contrast, excluding SSEs expands the highest hazard, highlighting their impact on hazard assessments (Figs 8 and 9). Our results indicate that the  $N_{\min}$  variation leads to higher accelerations and an increase in seismic hazard of up to ~70 per cent compared to the CRSHM 2022 for the Central Pacific and Osa Peninsula (Figs 8f and g). In contrast, the  $M_{\max}$  variation suggests a hazard reduction of ~10–15 per cent in the Nicoya Peninsula (Figs 9f and g). These outcomes emphasize the impact of geodetic data and the role of SSEs in modulating the spatial distribution of hazard levels.

To recap the previous outcomes and better quantify the effect of considering or not SSEs in the geodetic approach, we unify the results by weighting equally the  $N_{\min}$  and  $M_{\max}$  approaches (Fig. 7). Based on this, we obtain a final hazard map considering SSEs (Fig. 10a) or not (Fig. 10b). These maps show a wider extent of high accelerations when SSEs are excluded, especially in the Central Pacific region, with maximum PGAs up to 1.0 g, compared to 0.95 g when SSEs are included. To highlight these differences, we map the ratio between the accelerations of these maps (Fig. 10c), seeing that the inclusion of SSEs reduces the hazard along the peninsulas and the coast by up to ~10 per cent. PGA and ratio profiles in Fig. 10(d) quantify this impact beyond the hinterland, identifying negligible differences at ~150 km away from the trench.

#### 4.2. Main differences from the costa rica seismic hazard model 2022

Compared to CRSHM 2022, our results considering SSEs reveal two main hazard trends (Fig. 11a): (1) a decrease of up to 10 per cent in north-western Costa Rica, especially around the Nicoya Peninsula, and (2) a significant increase in the Central and Southern Pacific regions. In the latter, hazard levels rise by up to 40 per cent near the Central Pacific coast and 30 per cent near the Osa Peninsula. Notably, this increase extends inland, affecting central Costa Rica, including the capital city San Jose, where hazard levels rise by up to 10 per cent. The PGA and ratio profiles (Fig. 11b) allow us to identify the pattern of hazard calculations from the trench for the three segments evaluated. We observe decreases and/or increases in the seismic hazard, where the proportion of differences along the profiles is better shown. The differences become negligible beyond ~130 km for Nicoya, ~170 km for the Central Pacific and ~160 km for Osa. This observation is consistent with the MFD characterization of the segments (Fig. 6), with the Central Pacific segment being the one with the greatest differences with respect to the CRSHM 2022, followed by Osa and finally Nicoya.

#### 4.3. Hazard curves and disaggregation in key-sites

We selected key sites as San Jose (Fig. 11c), Nicoya (Fig. 11d), the Central Pacific (Fig. 11e) and Osa (Fig. 11f), to compare hazard curves from our calculations with those of the CRSHM 2022 for longer return periods, such as 2475 yr (equivalent to a 2 per cent probability of exceedance in 50 yr). Both models identify Nicoya

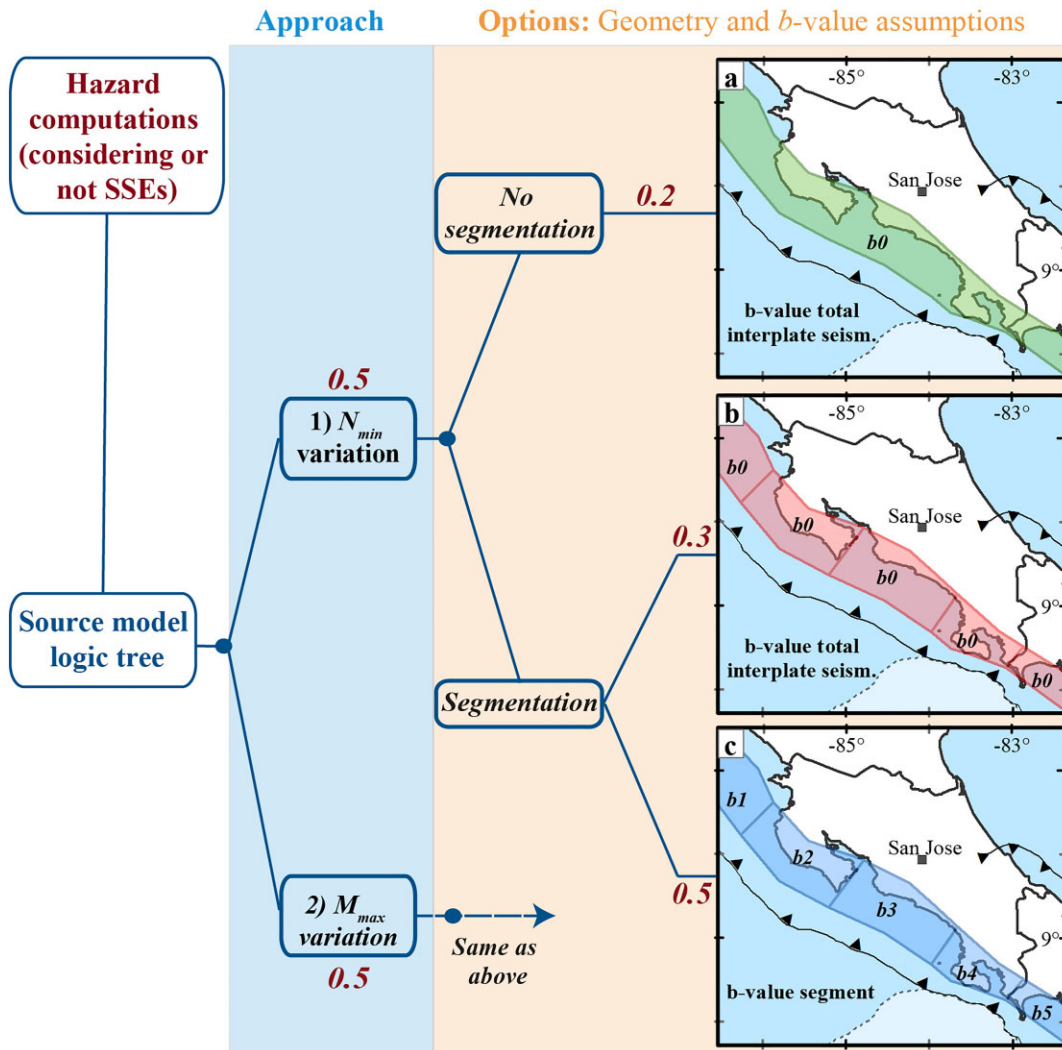


**Figure 7.** Logic tree for seismic hazard computations incorporating geodetic data. Weighting scheme of the different approaches and options of geometry and  $b$ -value.

as the highest hazard region, followed by Osa, while the Central Pacific and San José exhibit similar hazard levels. However, our geodetic model suggests comparable hazard levels for Nicoya and Osa, whereas the CRSHM 2022 estimates significantly higher hazard in Nicoya (Figs 11d and f).

Hazard curves in San José and Nicoya (Figs 11c and d) are similar between our calculations and CRSHM 2022, with slightly higher and lower hazard levels, respectively. These differences mostly fall in the 16th–84th percentile range of CRSHM 2022 and diminish for longer return periods, where the curves converge. Those small differences indicate that the variations are somehow covered by the epistemic uncertainty of the CRSHM 2022, mainly for high accelerations. For the Central Pacific and Osa (Figs 11e and f), there is an important increase in the hazard, much higher in our model than in the CRSHM 2022. In this case, the differences are significant and not covered by the epistemic uncertainty of the CRSHM 2022, restating the importance of considering a geodetic approach.

Additionally, we perform a hazard disaggregation in terms of magnitude-distance for an epsilon value of six. The epsilon value quantifies the deviation of ground motion intensity from the mean predicted by the ground motion model (McGuire 1995). In this case,

we fixed epsilon to focus the analysis specifically on the magnitude-distance pair. Applied to PGA-475 yr, this allows us to identify the main seismic sources contributing to the seismic hazard at the key sites (Fig. 11a). We explore this disaggregation for the CRSHM 2022 and for our results considering SSEs (see Fig. C5 in appendices). Then, to remark the differences in the pair magnitude-distance from one model to the other, we create contour maps per key site, based on the percentage of change in the contribution between both models (Fig. 12).

For San José, the seismic hazard is primarily controlled by upper-plate earthquakes ( $M_w$  5.0–6.5) at distances of 0–20 km. However, in our model, the contribution of upper-plate sources decreases, while the interplate sources such as Csi12 and Csi13 play a larger role (Fig. 12a). For Nicoya, hazard in both models are influenced by  $M_w$  6.5–8.0 events at 20–40 km, mainly from Csi11. In this site, differences between the models are small, with a slight decrease in the contribution from Csi11 and an increase from Csi12 and Csi13 in our model (Fig. 12b). In the Central Pacific and Osa, both models show interplate sources dominating at 15–40 km with  $M_w$  6.0–7.5. However, our model significantly increases the contributions from Csi12 and Csi13, while reducing those from upper-plate, other interplate, and in-slab sources (Figs 12c and d).

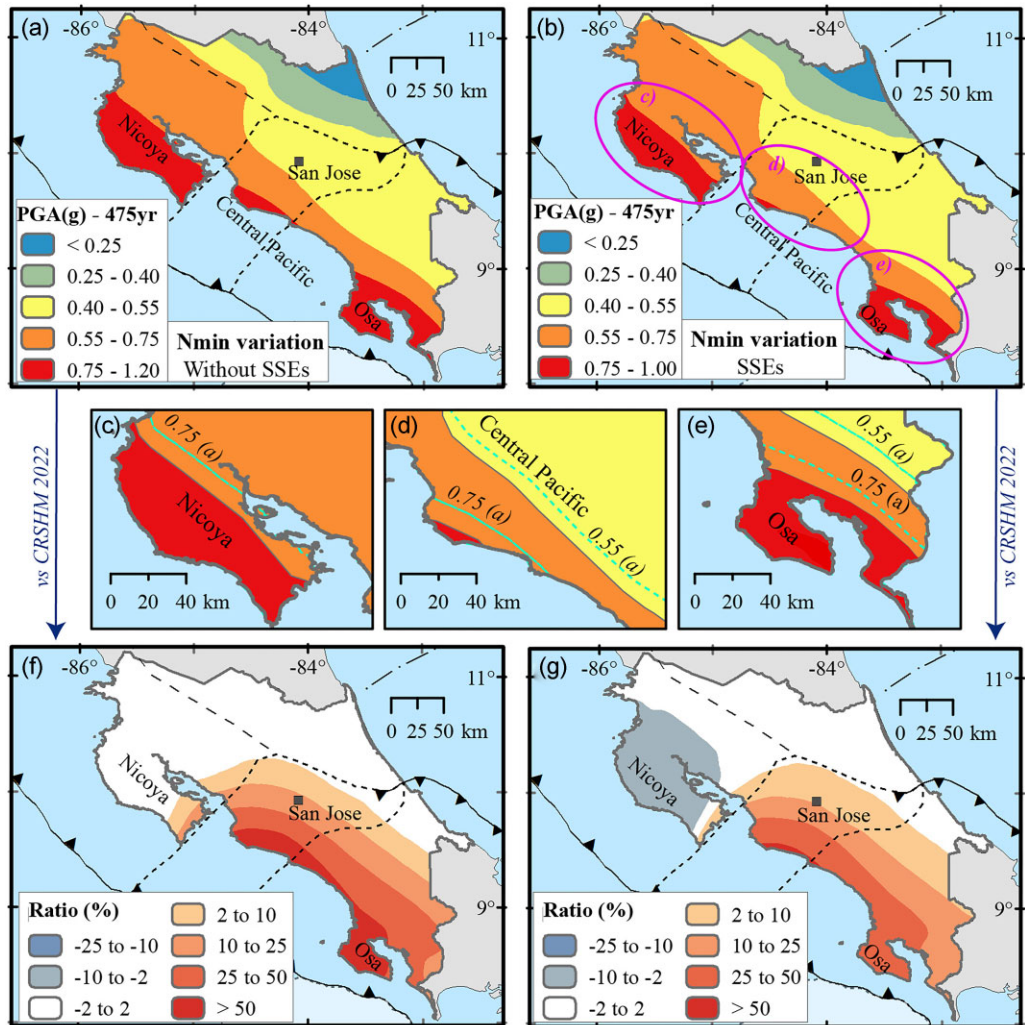


**Figure 8. Hazard computations for the  $N_{\min}$  approach.** (a) Without SSEs. (b) Considering SSEs. Ellipses in the panel (b) represent zoom areas where the variations between both computations for Nicoya are compared in panel (c), the Central Pacific (d) and Osa (e), respectively. Colours in panels (c)–(e) represent the hazard levels considering SSEs (same as b) and the dashed line represents the PGA isoline of the map in a (without SSEs). (f, g) Ratio of change respect to the CRSHM 2022: without SSEs (f) and considering SSEs (g).

## 5 DISCUSSION

### 5.1. Slip budget, coupling and large earthquakes in Nicoya and Osa

#### 5.1.1. Slip deficit analysis

We focus on the Nicoya and Osa peninsulas, where SSEs have been documented in Costa Rica (Figs 2 and 3b). In the SSE area below the Nicoya gulf, considering up to 250 mm of cumulative slip and assuming a convergence rate of 83 mm yr<sup>-1</sup> (DeMets *et al.* 2010), the slip deficit in the observational period of 6 yr is at most half than in the surroundings. In Nicoya, there are also important patches with cumulative slip from moderate SSEs at shallow depth (Voss *et al.* 2017) which, in conjunction with the deeper ones, may work as barriers, outlining areas prone to large earthquakes and where historical ruptures have occurred (Dixon *et al.* 2014; Obara & Kato 2016; Kato & Ben-Zion 2021). We find higher slip deficits in the shallow part of the interface than in the deep part. This observation

is consistent with Jiang *et al.* (2017), who stated that some portions of the shallow interface are strong enough to build up a slip deficit between frequent SSEs. Therefore, we do not discard the possibility of future ruptures to propagate in the up-dip direction, similar to the 2011  $M_w$  9.1 Tohoku-Oki Earthquake (Ide *et al.* 2011; Nishikawa *et al.* 2023).

In Osa, SSE patches are smaller than in Nicoya (Figs 2 and 3b) and are mostly located in the shallow part of the interface. Perry *et al.* (2023) reported that SSEs from 2018 to 2023 released a significant portion of the segment's budget, helping to accommodate accumulated deformation. A recurrence interval of 30–40 yr for large interplate earthquakes in Osa has been stated (Montero 1986; Protti *et al.* 1994). The last large earthquake occurred in 1983, therefore, nowadays there is a high probability of a major earthquake occurring there at any time. However, we consider that, in addition to a major earthquake in the up-dip region being less likely (Perry *et al.* 2023), its recurrence interval may be extended due to SSEs (Radiguet *et al.* 2012).

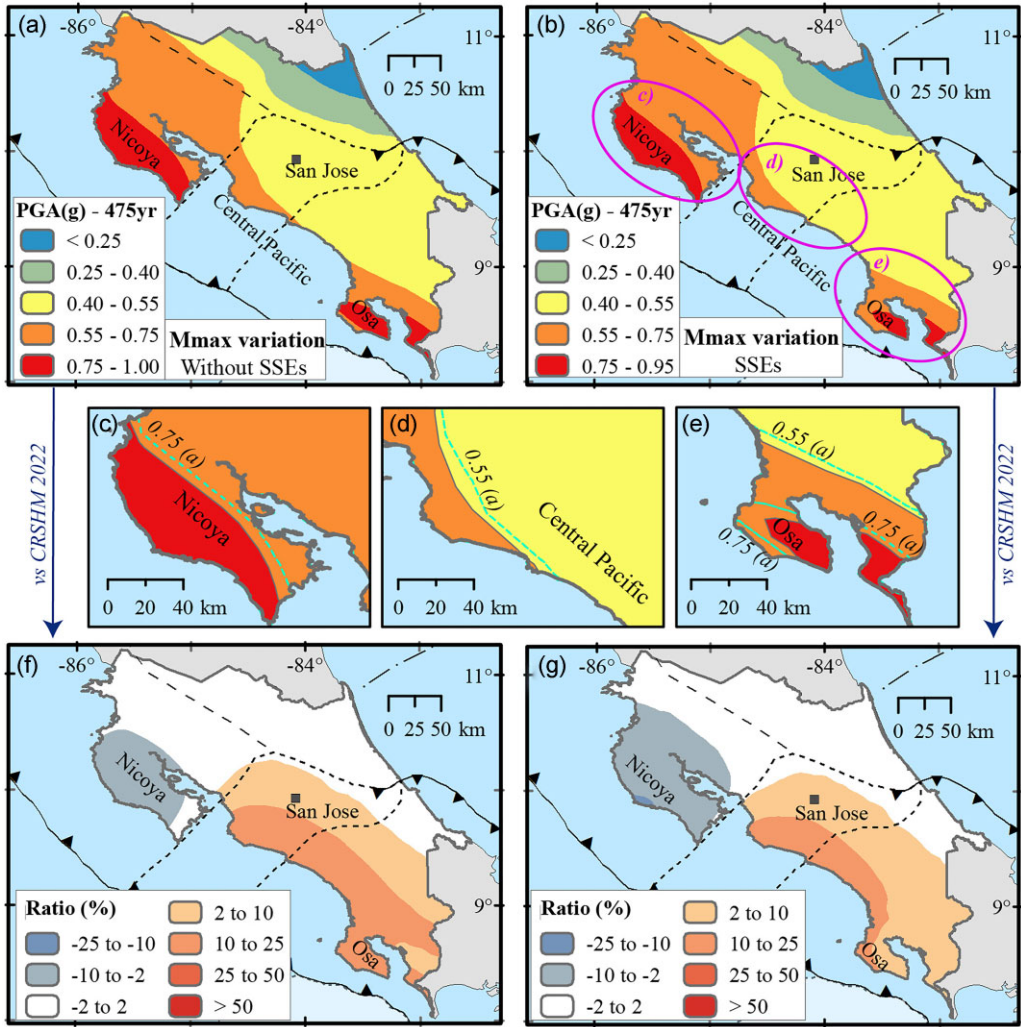


**Figure 9. Hazard computations for the  $M_{\max}$  approach.** (a) Without SSEs. (b) Considering SSEs. Ellipses in the panel (b) represent zoom areas where the variations between both computations for Nicoya are compared in panel (c), the Central Pacific (d) and Osa (e), respectively. Colours in panels (c)–(e) represent the hazard levels considering SSEs (same as b) and the dashed line represents the PGA isoline of the map in panel (a) (without SSEs). (f, g) Ratio of change respect to the CRSHM 2022: without SSEs (f) and considering SSEs (g).

### 5.1.2. Coupling and recurrence of large earthquakes

To quantify the proportion of slip rate accounting for SSEs, other aseismic processes (e.g. post-seismic and anelastic deformation), the recurrence of large earthquakes and how well these elements fit in Nicoya and Osa, we explore the model introduced by Zöller (2024). This model links the  $b$ -value from the GR relation with the coupling and the recurrence of large earthquakes, enabling the approximation of the seismic coupling coefficient ( $X$ ), based on the  $b$ -value ( $b$ ), and the coefficient of variation ( $C_v = S_d/R_p$ ) of the temporal series of large earthquakes, where  $S_d$  represents the standard deviation to the mean recurrence period ( $R_p$ ):

$$X = \frac{C_v}{\sqrt{\frac{b}{3-b}}} \quad (2)$$

Based on the updated and revised catalog presented by Arroyo-Solórzano & Linkimer (2021), we estimate the  $C_v$  values empirically (González *et al.* 2005) using the specific dates of events with  $M_w \geq 7.0$ . For Nicoya, using seven earthquakes between 1833 and 2012, we obtain a  $R_p = 30$  yr and  $S_d = 13.5$  yr. In Osa, considering six events between 1803 and 1983 we find a  $R_p = 36$  yr and

$S_d = 10.9$  yr. The  $C_v$  values obtained,  $b$ -values used, and resulting coupling factors are summarized in Table 5, and we also include the fraction of transient slip that is seismic ( $\alpha$ ) considering SSEs (see Section 3.2).

In Nicoya, the coupling closely matches our seismic transient slip fraction ( $\alpha$ ) and is similar to the values reported by Xue *et al.* (2015), suggesting that the incorporation of SSEs on the average seismic slip rates of the segment accurately represents the long-term coupling. This match of the long-term coupling with the SSEs areas has been also observed in Mexico, New Zealand and Chile (Plata-Martínez *et al.* 2021; Maubant *et al.* 2023; Jara *et al.* 2024). In Osa, the discrepancy between coupling and  $\alpha$  suggests either inaccuracies in estimating the segment's average loading rate (Avouac 2015) or the presence of several SSEs with  $M_w < 6.5$ , hidden in the geodetic noise (Jara *et al.* 2024). However, these coupling and  $\alpha$  values are within the typical range for megathrusts (0.5–0.8; Scholz & Campos 2012; Avouac 2015; Bürgmann 2018) supporting their consistency for hazard computations.

Additionally, we briefly explore the characteristic earthquake model (Youngs & Coppersmith 1985; Wesnousky 1986), which is a complementary way to evaluate the recurrence of large earthquakes.

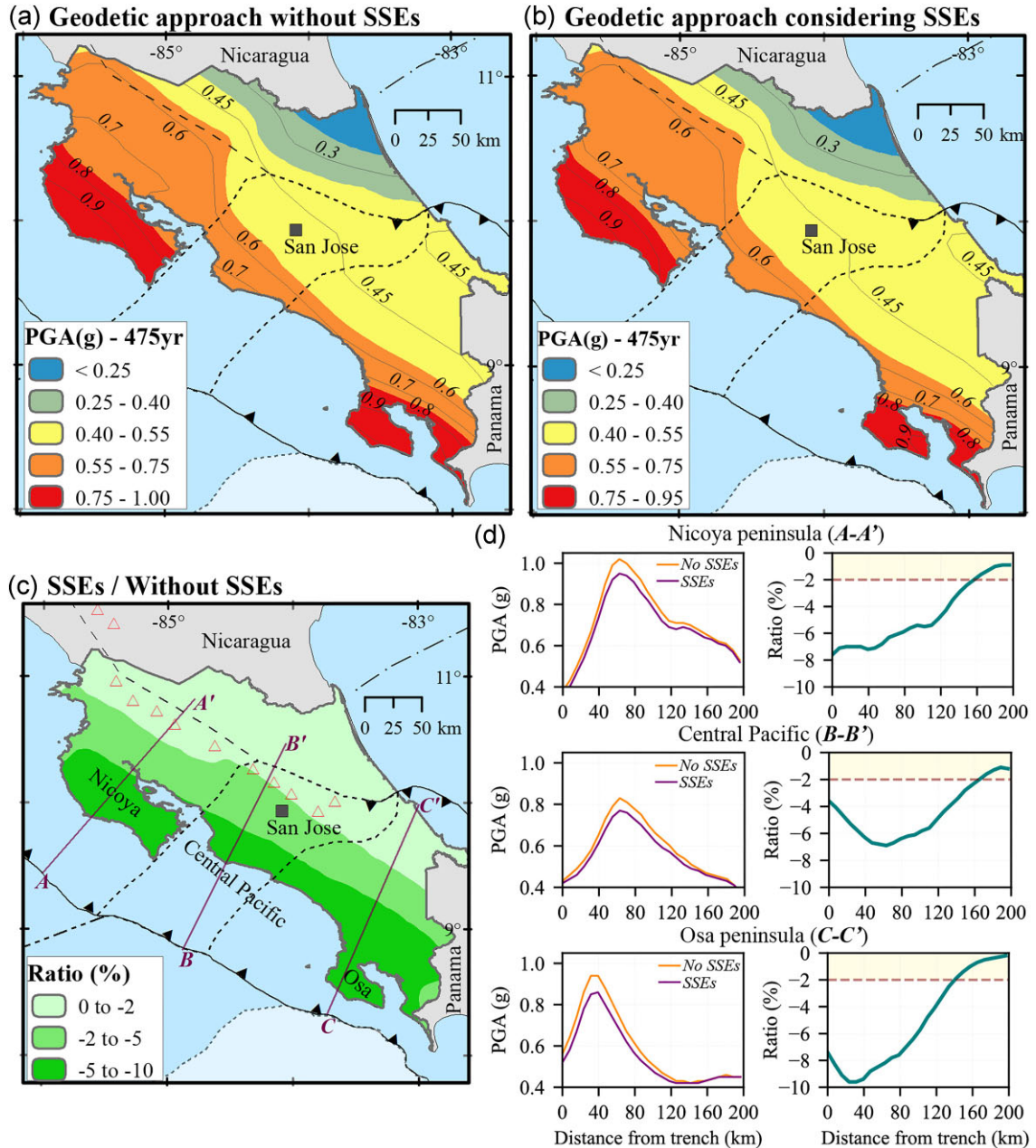


**Figure 10. Seismic hazard using geodetic information for the interplate sources.** (a) Without SSEs. (b) Considering SSEs. (c) Ratio map: SSEs/without SSEs. (d) PGA and ratio profiles per subduction segment for geodetic approaches. Lines in panel (c) represent the cross-sections in panel (d) and triangles in panel (c) represent the quaternary volcanoes.

In this case, if the interseismic strain is assumed to be accumulated and released only by the return of a characteristic earthquake of moment  $M_{oChar}$ , the average return period is explained as:

$$R_p(M_{Char}) = \frac{M_{oChar}}{\dot{M}_0} \quad (3)$$

Applying this to a  $M_{oChar}$  of  $M_w$  7.9 in Nicoya and  $M_w$  7.8 in Osa ( $M_{max}$  values calculated in Fig. 6), we used the relation from Hanks & Kanamori (1979) to convert from  $M_w$  to  $M_o$  to obtain the  $M_{oChar}$ . Considering the seismic slip rates from the inclusion of SSEs in the  $M_0$  of the seismogenic segments, this results in a  $R_p$  of 46 yr for Nicoya and 76 yr for Osa. These outcomes suggest that, if other large events ( $M_w > 7.0$ ) do not occur and energy accumulates for such magnitudes, the  $R_p$  could be delayed by ~16 yr in Nicoya

and up to ~40 yr in Osa, compared to our previous estimates, due to the release of aseismic energy from the SSEs. However, this approach is debatable when seismicity data covers only part of the interseismic period. Therefore, we recommend using instead physical simulations based on dynamic modelling of the seismic cycle (Avouac 2015; Rollins & Avouac 2019; Jiang *et al.* 2022; Li & Gabriel 2024).

### 5.1.3. Assumptions and limitations

A critical assumption in our study is that the seismogenic zone is fully coupled during inter-SSE periods (Avouac 2015). This assumption is actually not the real case in Costa Rica, as the coupling

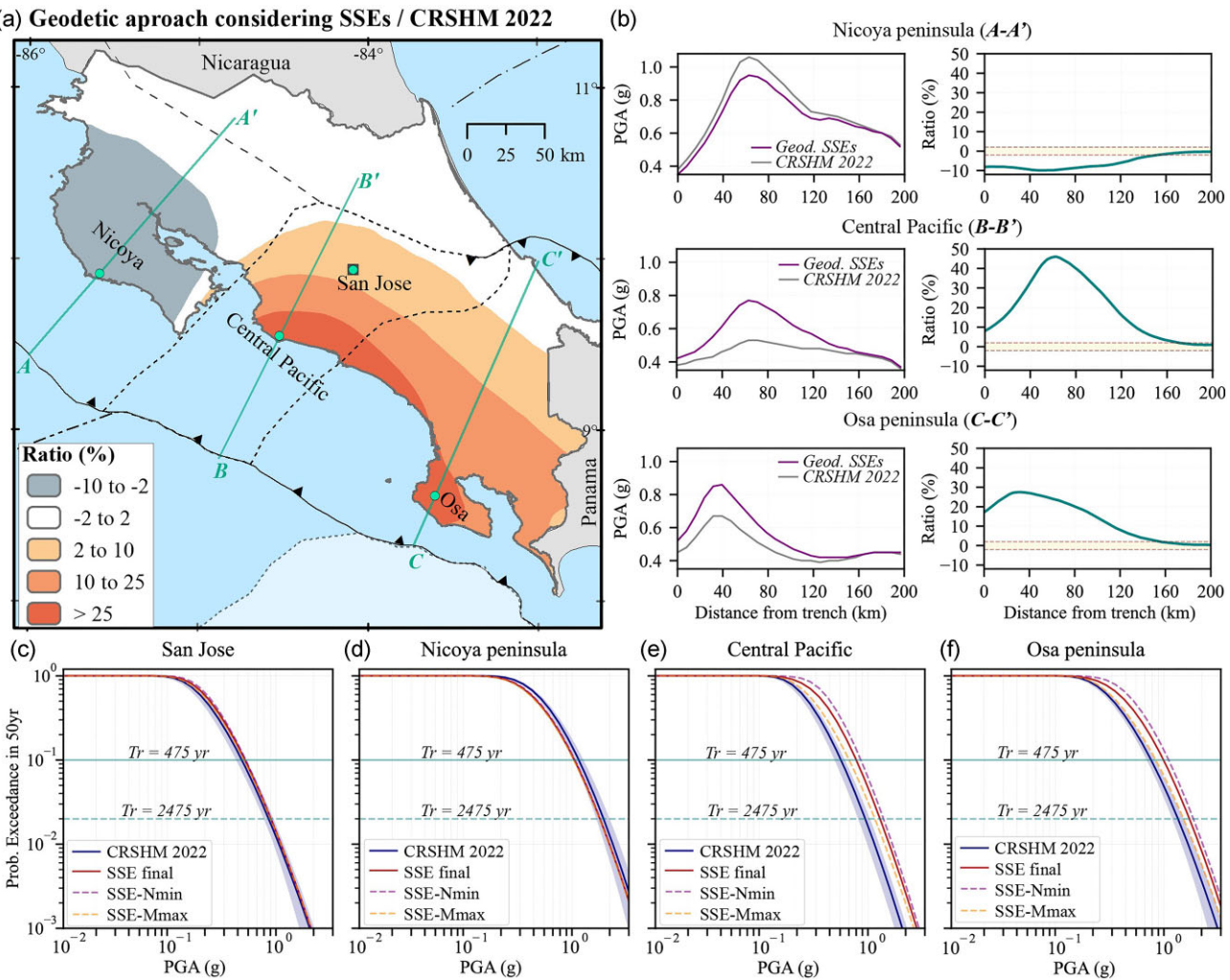


**Figure 11. Comparison with the CRSHM 2022.** (a) Ratio map: this study/CRSHM 2022. (b) PGA and ratio profiles per subduction segment. (c–f) Seismic hazard curves for the CRSHM 2022 and the geodetic approach in this study considering SSEs in specific locations: (c) San Jose, (d) Nicoya peninsula, (e) Central Pacific and (f) Osa peninsula. Lines in panel (a) represent the cross-sections shown in panel (b), and points are the specific inland locations for which we estimated the hazard curves. Shaded areas in panels (c)–(f) represent the 16th–84th percentile range of the hazard from the CRSHM 2022 for each site.

varies throughout the seismic cycle and spatially in Nicoya and Osa (Jiang *et al.* 2012, 2017; Perry *et al.* 2023). Nevertheless, we assume this behaviour in the long term, as well as the long-term slip rate on the interface is equal to the horizontal convergence rate across the plate boundary (Avouac 2015; Rollins & Avouac 2019). This supposition is also debatable, as it overlooks anelastic internal deformation and tectonic features like a tectonic sliver, which moves along the VAF at  $\sim 11 \text{ mm yr}^{-1}$  towards the northwest, parallel to the trench (Montero *et al.* 2017; Araya & Biggs 2020). Further relevant assumptions include that the historical catalog is complete and representative for  $M_w > 7.0$ , and that the MFD of largest events can be extrapolated from smaller ones using the GR relationship (Avouac 2015). However, large earthquakes may differ in MFD from smaller ones, with some studies suggesting a bimodal MFD and a  $b$ -value of  $\sim 1.5$  for the largest magnitudes (Yoder *et al.* 2012; Corral & González 2019; Chen *et al.* 2022).

A key limitation is the short geodetic monitoring period, which may not fully capture long-term coupling patterns. Additionally, our moment budget estimates rely on cumulative seismic slip rather than updated geodetic coupling models, which are crucial for refining hazard assessments by accounting for variations in fault locking

(Scotti *et al.* 2021; Tavakolizadeh *et al.* 2024). Another limitation is the exclusion of complex or multisegment ruptures along strike (Field *et al.* 2014; Chartier *et al.* 2019), which could increase  $M_{\max}$  (Schellart & Rawlinson 2013; Carvajal-Soto *et al.* 2020; Arroyo-Solórzano & Linkimer 2021). Future work could benefit from incorporating earthquake physics and rupture probabilities across aseismic barriers (Rollins & Avouac 2019; Michel *et al.* 2023). Despite these limitations, our model marks a significant improvement by integrating both seismic and geodetic data (not applied in the CRSHM 2022), providing a more comprehensive assessment of stress load and release along the subduction interface.

## 5.2. Integrating geodetic data and slow-slip events on PSHA

### 5.2.1. Primary influence on seismic hazard of the interplate sources

To assess the impact of interplate sources on seismic hazard and the influence of our geodetic model with SSEs, we disaggregate the hazard by seismic sources for both our model and CRSHM

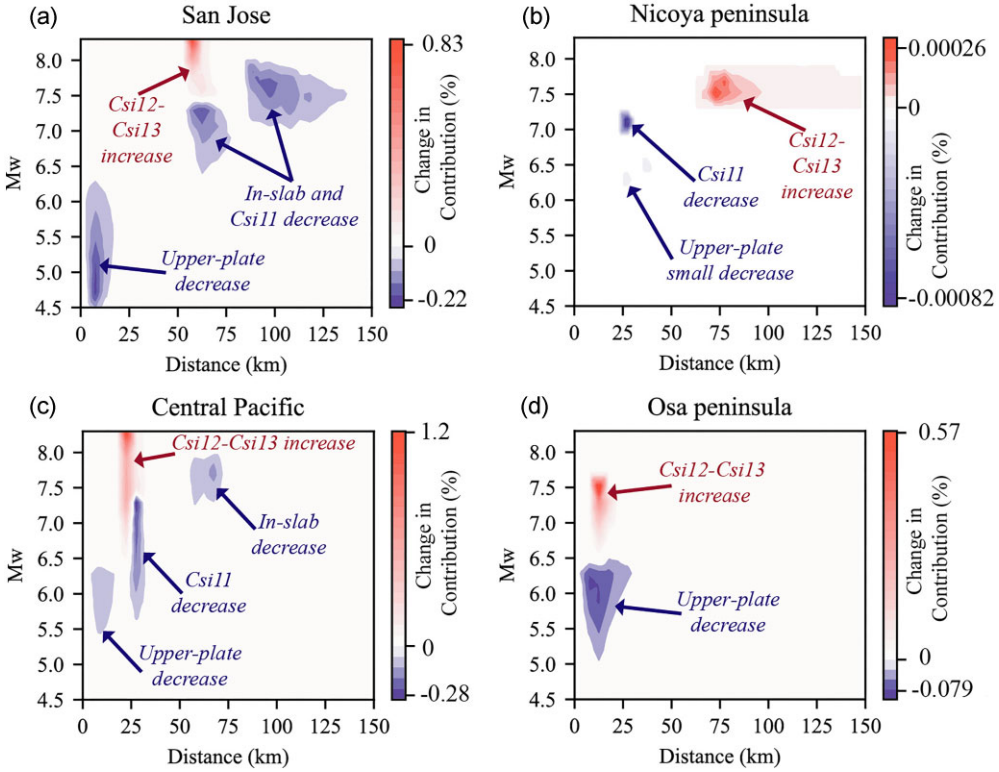


**Figure 12.** Differences in the  $M_w$ -distance disaggregation results from this study with respect to the CRSHM 2022. The sites are the same as in Fig. 11(a): San Jose (a), Nicoya peninsula (b), Central Pacific (c) and Osa peninsula (d).

**Table 5.** Non-geodetic coupling factors ( $X$ ) obtained based on the Zoller (2024) relationship, and fraction of transient slip that is seismic ( $\alpha$ ) obtained from the geodetic analysis for Nicoya and Osa.

Region	$C_v$	$b$ -value	$X$ from equation (2)	$\alpha$
Nicoya (Csi11)	0.45	0.69	0.82	0.79
Osa (Csi13)	0.30	0.84	0.48	0.64

2022 (see full results in Fig. C6, appendices). This analysis, conducted for key sites in Fig. 11(a), separates source contributions to PGA based on their mean annual earthquake rates. Defined sources include the segments in Nicoya (Csi11), Central Pacific (Csi12) and Osa (Csi13), along with grouped sources by tectonic regime: upper-plate, in-slab, and other interplate sources from Nicaragua and Panama. A heatmap (Fig. 13) illustrates the percentage change in source contributions between our model and CRSHM 2022. Our model shows notable contribution changes with respect to CRSHM 2022, particularly in the increased influence of Csi12 at sites in San José and the Central Pacific (Fig. 13). Moreover, while the hazard pattern in our model follows the CRSHM 2022, acceleration values increase, particularly due to adjustments in the Csi12 source, which also affect contributions from upper-plate and in-slab sources.

Another remarkable feature is the effect of SSEs and the non-segmentation assumption. At Nicoya and Osa (Fig. 13), the impact of Csi11 and Csi13 decreases, with greater contributions from neighbouring interplate sources (e.g. Nicaragua and Panama), suggesting that interplate sources could rupture together in a non-segmented scenario. Schellart & Rawlinson (2013), suggested by analogy with the tectonic settings of the mega earthquakes in Chile (1960), Alaska (1964) and Sumatra (2004), that in Costa Rica a potential rupture could initiate in Osa and propagate towards the northwest. Additionally, the reduced contribution from Csi11 in Nicoya and Csi13 in Osa at high PGA (Fig. 13) is associated with

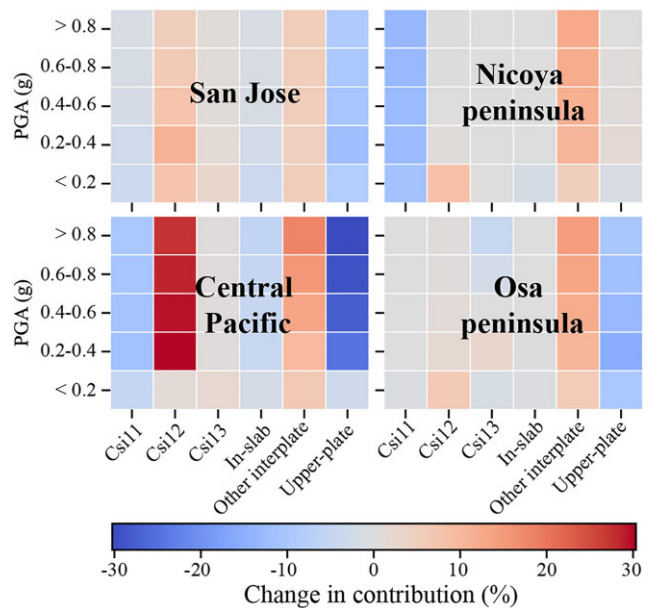


**Figure 13.** Differences in sources contribution from this study with respect to the CRSHM 2022. The sites are the same as in Fig. 11(a): San Jose (a), Nicoya peninsula (b), Central Pacific (c) and Osa peninsula (d).

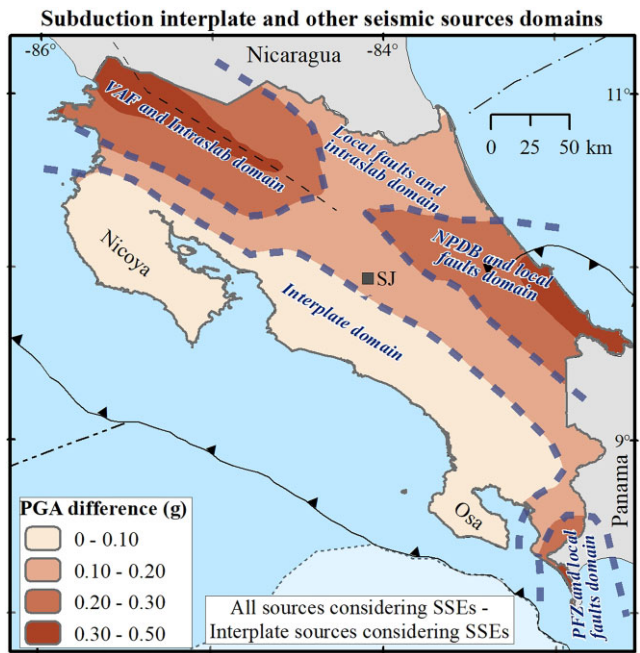


**Figure 14. Hazard domains of seismic sources.** The colours show the differences between hazard computations considering SSEs with all the seismic sources of Costa Rica and only with interplate sources. Dashed lines highlight the main domains per seismic source based on their contribution in the final seismic hazard results.

the geodetically determined  $M_{\max}$ , including SSEs, in both peninsulas. These regions offer good conditions for geodetic and SSE monitoring, enhancing  $M_{\max}$  constraints (Xie *et al.* 2020; Perry *et al.* 2023).

We also investigate the differences in hazard calculations by comparing results using all sources (interplate, upper-plate and in-slab) versus only interplate sources. The differences between these calculations are analysed through residuals (see Fig. C7 in the appendices). The final difference map, considering SSEs, is shown in Fig. 14. This map highlights areas where the hazard increases due to non-interplate sources (high differences) and regions where interplate sources dominate the hazard (low differences). Interplate sources predominantly influence the hazard along the Pacific coast, extending up to 70 km inland from the peninsulas and about 50 km from the rest of the coast. This pattern narrows to the north and is interrupted in the south due to the Panama Fracture Zone and crustal faults near the Panama border.

In addition to the interface influence, we highlight other tectonic features (Fig. 1), particularly fault zones contributing to seismic hazard (Fig. 14). First, large differences align with the VAF, where several major faults are located (Montero *et al.* 2017; Araya & Biggs 2020). Second, the NPDB also plays a significant role, suggested as an emerging subduction zone (Bourke *et al.* 2023). Moreover, the PFZ and crustal faults account for much of the seismicity in the southern Pacific region (Morell *et al.* 2008; Arroyo & Linkimer 2021). In contrast, deformation zones with several faults, like the CCRDB, do not generate hazard domains. This is likely due to seismic zoning (Alvarado *et al.* 2017) and to not treating faults as independent sources, which would lead to higher accelerations in their vicinity (Rivas-Medina *et al.* 2018; Chartier *et al.* 2019; Scotti *et al.* 2021).

### 5.2.2. Challenges and updates for Costa Rica

If the earthquake catalogue and SSE observations covered long timespans, our model (including SSEs and geodetic data) would likely align with CRSHM 2022 (based solely on seismic catalogue information), with comparable seismic moment rates. However, differences may arise due to regional variations in geodetic monitoring and the completeness of the earthquake catalogue.

Geodetic observations are crucial to detect and monitor aseismic processes. In Nicoya, several studies on SSEs using geodetic data have been conducted since the early 2000s (Ghosh *et al.* 2008; Dixon *et al.* 2014; Chaves *et al.* 2017; Jiang *et al.* 2017; Voss *et al.* 2018; Xie *et al.* 2020). In contrast, geodetic coverage in the Central Pacific is limited, and the monitoring in Osa began to improve in 2018 (Perry *et al.* 2023). A short seismic instrumental record also limits the ability to fully capture the seismic cycle of large earthquakes, while historical and macroseismic records often contain gaps and uncertainties. In Costa Rica, the catalogue of large earthquakes ( $M_w > 7.0$ ) is more complete for Nicoya (Figs 1 and 2a), where better geodetic monitoring helps constrain both seismicity and geodetic information. In contrast, the Central Pacific has more uncertainties, with Osa representing an intermediate case (Fig. 6).

The challenges in reconciling seismicity with the slip deficit in the Central Pacific (Figs 6c and d) may be due to incomplete records of large earthquakes or variations in coupling. These issues could suggest a longer seismic cycle for events above  $M_w 7.0$  or the accommodation of some convergence through other processes, like intraplate deformation. A transition zone in the Central Pacific region shows increasing rates and depth of seismicity from the southern (Osa) to the northern part (Bourke *et al.* 2020; Arroyo-Solórzano & Linkimer 2021), likely due to differences slab depth, bathymetry, geometry (Protti *et al.* 1994; Arroyo *et al.* 2014; Lücke & Arroyo 2015). These differences might contribute to diverse coupling behaviour, potentially leading to more intraplate deformation. This deformation may also transfer stress to the upper plate of the Central Pacific, where large faults, deep crustal earthquakes and a tectonic sliver are present (Montero 2001; Pacheco *et al.* 2006; Mescua *et al.* 2017; Porras *et al.* 2021). These factors, along with limited geodetic data coverage, explain the challenges in reconciling the observed seismicity with geodetic estimates of the moment budget in the Central Pacific segment.

Considering the results from our model, we revisit the tectonic hazard zonation proposed by Hidalgo-Leiva *et al.* (2023). Their four-category model (moderate, high, very high and extremely high seismic hazard) lacked clear distinctions between the very high and extremely high hazard categories. In contrast, our results provide better differentiation, using the same tectonic features but refining the hazard categories based on PGA. Peninsulas are now better differentiated, corresponding to the 0.7–1.0 g (Fig. 10) PGA range, as extremely high hazard. We also redefine the high hazard category, using the 0.55–0.70 g range as a reference, extending it along the Pacific coast, in line with the interplate source domain (Fig. 14), rather than limiting it to the northern part. Lastly, by keeping the PGA ranges of 0.40–0.55 g for high hazard and <0.40 g for moderate hazard, the high hazard no longer extends to the Pacific coast (now categorized as very high hazard), while moderate hazard is now confined to the back-arc region.

### 5.2.3. Epistemic uncertainty framework

We organize key assumptions and limitations within the framework of epistemic uncertainty related to our geodetic approach for seismic

source models in PSHA. We focus on primary parameters such as source geometry,  $b$ -value, moment rate ( $\dot{M}_0$ ) and seismic slip rates ( $\dot{s}$ ), as well as secondary inputs that are relevant to defining the primary parameters, such as shear modulus ( $\mu$ ), convergence rate and coupling or slip deficits. Moreover, it is important to note that our geodetic approach still depends, to some extent, on seismic catalogue information, such as with the  $b$ -value.

We applied two distinct approaches, evaluating variations in  $N_{\min}$  and  $M_{\max}$ , to balance the moment rate (Fig. 4). For the first approach, setting  $N_{\min}$  based on observed catalogue seems uncontroversial, but fixing  $M_{\max}$  is a topic of debate. Bungum (2007) suggested that moment release is more sensitive to  $M_{\max}$  than  $N_{\min}$ . However, our findings indicate this is not always the case (Figs C1–C4 in appendices). With this in mind, a logic tree sketch for our model includes three main branches: the source geometry,  $b$ -values, and  $\dot{M}_0$ . For the  $N_{\min}$  approach, there is also the possibility of an additional branch for  $M_{\max}$ , but in our study this is fixed at a single magnitude.

For source geometries, we assign weights based on the acceptance of segmentation along Costa Rica's subduction interface (Protti *et al.* 1994)), with 0.8 for segmentation and 0.2 for unsegmented (Fig. 4). Geometry influences the geodetic  $\dot{M}_0$ , the proximity of ruptures to the surface, and  $M_{\max}$  variation. In our  $M_{\max}$  approach, unsegmented interfaces yield larger ruptures with greater hazard impact, while segmented assumptions show that  $N_{\min}$  can yield higher accelerations when  $M_{\max}$  is fixed (Appendix C). Similar differences have been observed in other studies (Field *et al.* 2014; Visini *et al.* 2020; Scotti *et al.* 2021). For a better control of epistemic uncertainties on the geometry definition, we recommend using updated models while considering multiple, less-probable ruptures with lower weights.

The  $b$ -value is influenced by source geometry, which defines the seismicity used for its estimation. We use  $b$ -values from Arroyo-Solorzano and Linkimer (2021), assigning a weight of 0.2 for the no-segmentation case. For segmentation, we applied either the total interpolate  $b$ -value to each segment (weight of 0.3) or a segment-specific  $b$ -value (weight of 0.5), resulting in a global weight of 0.5 for both approaches. In our geodetic approach the  $b$ -value is critical for balancing the moment budget when  $M_{\max}$  is fixed. It influences results by increasing  $N_{\min}$  for large magnitudes or by guiding potential  $M_{\max}$  values based on catalogue comparisons (Figs 4a and b). In Nicoya, our results align with the catalogue, but differences arise in the Central Pacific and Osa regions, highlighting the importance of  $b$ -value in closing the moment budget (Fig. 6). To reduce epistemic uncertainty, future studies should consider applying multiple methods for the  $b$ -value estimation.

$\dot{M}_0$  is typically estimated using eq. (1). While some studies suggest ways to constrain seismic and geodetic data for its estimation (Bird *et al.* 2015; Kagan & Jackson 2016; Bayona *et al.* 2021; Michel *et al.* 2021, 2023), we follow a purely geodetic approach, where the  $\dot{M}_0$  is determined by the area,  $\mu$ , and  $\dot{s}$ . The area is defined by the established geometry, emphasizing the influence of source geometry on epistemic uncertainty. Regarding  $\mu$ , we assumed a value of 30 GPa (Wells & Coppersmith 1994), but variations in  $\mu$  have been suggested for Central America (Arroyo-Solórzano *et al.* 2024), so alternatives in the future should be considered to account for epistemic uncertainty.

For seismic slip rates ( $\dot{s}$ ), we account for SSEs using convergence rates and slip deficit (Section 3.1). We use convergence rates from the PVEL model (DeMets *et al.* 2010), which specifies the motion of the Cocos plate relative to the Caribbean plate, instead of, for instance, the global MORVEL model (DeMets *et al.* 2010). However, using alternative plate velocity models could be considered

by using weighting schemes, introducing different branching levels that could be analysed alongside slip deficit estimations. Regarding slip deficit, better control of uncertainties could be incorporated by estimating coupling maps based on Bayesian techniques (Jolivet *et al.* 2020; Jara *et al.* 2024)), introducing probability distributions, adding up to three more branches for  $\dot{s}$  estimation. Hence, for the  $\dot{s}$  estimation up to six branches could be considered, accounting different convergence rates models and slip deficit/coupling analysis. However, it is important to emphasize that the influence of  $\dot{s}$  is primarily reflected in the seismic moment rate ( $\dot{M}_0$ ), which depends on rigidity ( $\mu$ ) and source area. This observation highlights that the differences between our results and CRSHM 2022 arise mainly from the geodetic approach, with SSE inclusion playing a secondary role.

We mitigate the epistemic uncertainty associated through the evaluation of the  $N_{\min}$  and  $M_{\max}$  approaches. However, epistemic uncertainty remains due to data limitations or assumptions. In our model, epistemic uncertainty is largely managed by source geometry, with  $b$ -value influencing it secondarily. Accordingly, our logic tree (Fig. 7) includes six branches: two of the different approaches ( $N_{\min}$  and  $M_{\max}$ ) and three combining the options of geometry and  $b$ -values. This scheme is complemented by a fixed  $\dot{M}_0$ , assuming a sole possible value for  $\mu$  and for the  $\dot{s}$ , this latter based on a detailed analysis of SSEs.

To further reduce epistemic uncertainty, refining the  $\dot{M}_0$  estimation is essential. This process would involve adding more branches to the logic tree, considering alternative assumptions for  $\mu$ , convergence rates and coupling maps with probabilistic distributions. Moreover, enhanced geodetic data through more observations and instrumentation would improve reliability and reduce uncertainty. Additionally, incorporating alternative seismic zoning models could further reduce epistemic uncertainty.

## 6 CONCLUSIONS

We propose a methodology to incorporate geodetic data, and, in particular, the information from SSEs into PSHA by exploring different methods to convert moment rate budgets into earthquake rates and maximum magnitudes ( $M_{\max}$ ). While previous studies have explored including aseismic processes in earthquake rates or in determining  $M_{\max}$ , our approach is the first to evaluate both within a seismic hazard framework, uniquely focusing on SSEs and rigorously addressing epistemic uncertainties. This approach allows robust hazard assessments and provides a reference framework for future characterizations of seismic source models in seismic hazard.

We found that PSHA based on geodetic data leads to higher ground motion levels when SSEs are disregarded. Furthermore, when comparing our results with the Costa Rica Seismic Hazard Model 2022 (CRSHM 2022, Hidalgo-Leiva *et al.* 2023), there is not a unique trend of seismic hazard results either increasing or decreasing. We show that the geodetic approach considering SSEs in Costa Rica result in hazard decreases of up to  $\sim 15$  per cent in the Nicoya Peninsula and increases of up to  $\sim 40$  per cent in the Central Pacific region and  $\sim 30$  per cent in the Osa Peninsula. These variations may be associated with the variable earthquake catalogue completeness and geodetic data monitoring along the subduction interface in Costa Rica.

The slip deficits in the SSE patches in Nicoya are half those of the surrounding coupled seismogenic zone, potentially acting as barriers to large earthquakes. In Osa, the probability of a major

earthquake is high due to the time since the last one, but the recurrence period may be being extended by the SSEs. In addition, our findings on seismic coupling based on mean recurrence periods and  $b$ -values suggest that coupling in Nicoya aligns well with the seismic slip fraction, while in the other regions it may be underestimated due to unaccounted SSEs, catalogue bias or intraplate deformation. We also identified that the interplate sources control the hazard along the Pacific coast, extending inland up to 70 km with some differences towards the north and south, where other tectonic features and active crustal faults are major contributors to the hazard.

Our models strongly depend on the source geometry, the  $b$ -value, and the moment rate. Therefore, it is essential to reassess periodically seismic recurrence parameters ( $b$ -value,  $M_{\max}$ ,  $N_{\min}$ ) and subduction interface geometry. Additionally, it is relevant to explore different approaches to evaluate the consistency of the aseismic processes and to assess long-term earthquake rates and the  $M_{\max}$  from moment rate budgets. We suggest that hazard modellers might include in their logic trees both approaches based on seismic catalogs and seismic slip rate data (geological/geodetic). This complementary analysis will account for aseismic processes not reflected in the catalog and address better the epistemic uncertainties in methods and data. Moreover, we recommend future research to improve the integration of SSEs in hazard by including more observations and incorporating updated coupling maps.

This work represents an important step towards more robust and realistic frameworks for seismic risk mitigation. Furthermore, our results serve as a starting point for more accurate future seismic hazard assessments in Costa Rica and other regions where SSEs frequently occur. Finally, by improving the understanding of aseismic processes and their physical influence, we also underscore the importance and impact of incorporating geodetic data into PSHA.

## DATA AVAILABILITY

The seismic catalogue was obtained from the National Seismological Network of Costa Rica (RSN); <http://www.rsn.ucr.ac.cr>, doi:10.15517/TC (last accessed September 2024), and the GNSS time-series for the stations PUJE and RIOS used for the plots were obtained from the Nevada Geodetic Laboratory (<https://geodesy.unr.edu/NGLStationPages/GlobalStationList>). Seismic hazard calculations were performed using the OpenQuake engine (<https://github.com/gem/oq-engine>). The seismic hazard model is based on the 2022 Seismic Hazard Model for Costa Rica (Hidalgo-Leiva *et al.* 2023), with the changes to the source model detailed in the manuscript and Appendix B. All input files and main outputs are available in a public repository (<https://data.mendeley.com/datasets/7x8xv2yf23/2>) for the hazard computations in OpenQuake and the main outputs (e.g. hazard maps and ground motion grids, hazard curves and disaggregation). Appendices comprise of three parts to complement the main article and provide readers with an open review of the calculations performed: (A) catalogue of SSEs in Costa Rica, (B) MFD characterization details and (C) complementary seismic hazard computations.

## ACKNOWLEDGMENTS

Special thanks to the Associate Editor Eiichi Fukuyama, to the reviewer David Small and the anonymous referee for their comments and suggestions, which improved the article. Thanks also to Dr Laura Wallace, Dr José Antonio Bayona and Dr Romain

Jolivet for enlightening discussions and valuable feedback. M. Arroyo-Solórzano acknowledges the funding programme number 57645448 from the Deutscher Akademischer Austauschdienst (DAAD). J. Jara acknowledges an MSCA Postdoctoral Fellowship (MSCA-101066069, project ERASMUS). Á. González was funded by two grants of the Spanish Research Agency (agency code MCIN/AEI/10.13039/501100011033): IJC2020-043372-I (supported by the European Union NextGenerationEU/PRTR) and PID2021-125979OB-I00 (supported by the European Union ERDF). D. Hidalgo-Leiva acknowledges to the University of Costa Rica through the project referenced as C4-900.

## AUTHOR CONTRIBUTIONS

M. Arroyo-Solórzano designed the study, processed the data, made the figures and wrote the paper with contributions from all co-authors. All the authors interpreted, discussed and analysed the results and revised the article. The authors also acknowledge that there are no conflicts of interest recorded.

## SUPPORTING INFORMATION

Supplementary data are available at [GJI/GAA342](https://doi.org/10.1093/gji/gjaa342) online.

Please note: Oxford University Press is not responsible for the content or functionality of any supporting materials supplied by the authors. Any queries (other than missing material) should be directed to the corresponding author for the paper.

## REFERENCES

- Adamek, S.,** Frohlich, C. & Pennington, W.D., 1988. Seismicity of the Caribbean-Nazca boundary: constraints on microplate tectonics of the Panama region, *J. geophys. Res.*, **93**, 2053–2075.
- Allen, T.I. & Hayes, G.P.,** 2017. Alternative rupture-scaling relationships for subduction interface and other offshore environments, *Bull. seism. Soc. Am.*, **107**, 1240–1253.
- Alvarado, G.E. *et al.*,** 2017. The new Central American seismic hazard zonation: mutual consensus based on up to day seismotectonic framework, *Tectonophysics*, **721**, 462–476.
- Anderson, J.G. & Luco, J.E.,** 1983. Consequences of slip rate constraints on earthquake occurrence relations, *Bull. seism. Soc. Am.*, **73**, 471–496. Retrieved from <http://pubs.geoscienceworld.org/bssa/bssa/article-pdf/73/2/471/5331484/bssa0730020471.pdf>
- Araya, M.C. & Biggs, J.,** 2020. Deformation associated with sliver transport in Costa Rica: seismic and geodetic observations of the July 2016 Bijagua earthquake sequence, *Geophys. J. Int.*, **220**, 585–597.
- Arroyo-Solórzano, M. & Linkimer, L.,** 2021. Spatial variability of the  $b$ -value and seismic potential in Costa Rica, *Tectonophysics*, **814**, 228–951. doi:10.1016/j.tecto.2021.228951.
- Arroyo-Solórzano, M., Benito, M.B., Alvarado, G.E. & Climent, A.,** 2024. Empirical earthquake source scaling relations for maximum magnitudes estimations in Central America, *Bull. seism. Soc. Am.*, **114**, 1539–1567.
- Arroyo, I.G. & Linkimer, L.,** 2021. Geometría de la zona sismogénica interplacas en el sureste de Costa Rica a la luz de la secuencia sísmica de Golfito del 2018, *Geofis. Int.*, **60**, 51–75.
- Arroyo, I.G., Husen, S. & Flueh, E.R.,** 2014. The seismogenic zone in the Central Costa Rican Pacific margin: high-quality hypocentres from an amphibious network, *Int. J. Earth Sci.*, **103**, 1747–1764.
- Avouac, J.P.,** 2015. From geodetic imaging of seismic and aseismic fault slip to dynamic modeling of the seismic cycle, *Annu. Rev. Earth Planet. Sci.*, **43**, 233–271.
- Baba, S., Obara, K., Takemura, S., Takeo, A. & Abers, G.A.,** 2021. Shallow slow earthquake episodes near the trench axis off Costa Rica, *J. Geophys. Res. Solid Earth*, **126**, doi:10.1029/2021JB021706.

- Bayona, J.A.**, Savran, W., Strader, A., Hainzl, S., Cotton, F. & Schorlemmer, D., 2021. Two global ensemble seismicity models obtained from the combination of interseismic strain measurements and earthquake-catalogue information, *Geophys. J. Int.*, **224**, 1945–1955.
- Benito, M.B.** *et al.*, 2012. A new evaluation of seismic hazard for the Central America region, *Bull. seism. Soc. Am.*, **102**, 504–523.
- Bird, P.**, Jackson, D.D., Kagan, Y.Y., Kreemer, C. & Stein, R.S., 2015. GEAR1: a global earthquake activity rate model constructed from geodetic strain rates and smoothed seismicity, *Bull. seism. Soc. Am.*, **105**, 2538–2554.
- Bourke, J.**, Levin, V., Linkimer, L. & Arroyo, I., 2020. A recent tear in subducting plate explains seismicity and upper mantle structure of Southern Costa Rica, *Geochem. Geophys. Geosyst.*, **21**, doi:10.1029/2020GC009300.
- Bourke, J.R.**, Levin, V., Arroyo, I.G. & Linkimer, L., 2023. Evidence for Caribbean plate subduction in southern Costa Rica, *Geology*, **51**, 408–412.
- Brune, J.N.**, 1968. Seismic moment, seismicity, and rate of slip along major fault zones, *J. geophys. Res.*, **73**, 777–784.
- Bungum, H.**, 2007. Numerical modelling of fault activities, *Comput. Geosci.*, **33**, 808–820.
- Bürgmann, R.** & Thatcher, W., 2013. Space geodesy: a revolution in crustal deformation measurements of tectonic processes, *Special Paper of the Geological Society of America*, **500**, 397–430.
- Bürgmann, R.**, 2018. The geophysics, geology and mechanics of slow fault slip, *Earth planet. Sci. Lett.*, **495**, 112–134.
- Calderon, A.** & Silva, V., 2019. Probabilistic seismic vulnerability and loss assessment of the residential building stock in Costa Rica, *Bull. Earthq. Eng.*, **17**, 1257–1284.
- Carvajal-Soto, L. A.**, Ito, T., Protti, M. & Kimura, H., 2020. Earthquake potential in Costa Rica using three scenarios for the central Costa Rica deformed belt as western boundary of the Panama microplate, *J. of South American Earth Sci.*, **97**, doi:10.1016/j.jsames.2019.102375.
- Chartier, T.**, Scotti, O. & Lyon-Caen, H., 2019. Sherifs: open-source code for computing earthquake rates in fault systems and constructing hazard models, *Seismol. Res. Lett.*, **90**, 1678–1688.
- Chaves, E.J.**, Duboeuf, L., Schwartz, S.Y., Lay, T. & Kintner, J., 2017. Aftershocks of the 2012 Mw 7.6 Nicoya, Costa Rica, earthquake and mechanics of the plate interface, *Bull. seism. Soc. Am.*, **107**, 1227–1239.
- Chen, S.K.**, Wu, Y.M. & Chan, Y.C., 2022. The seismogenic potential of the southernmost Ryukyu Subduction Zone as revealed by historical earthquakes and slow slip events, *Front. Earth Sci. (Lausanne)*, **10**, doi:10.3389/feart.2022.887182.
- Cornell, A.**, 1968. Engineering seismic risk analysis, *Bull. seism. Soc. Am. (BSSA)*, **58**, 1583–1606.
- Corral, Á.** & González, Á., 2019. Power law size distributions in geoscience revisited, *Earth Space Sci.*, **6**, 673–697.
- Cruz-Atienza, V.M.** *et al.*, 2021. Short-term interaction between silent and devastating earthquakes in Mexico, *Nat. Commun.*, **12**, doi:10.1038/s41467-021-22326-6.
- Dascher-Cousineau, K.** & Bürgmann, R., 2024. Global subduction slow slip events and associated earthquakes, *Sci. Adv.*, **10**, doi:10.1126/sciadv.ado2191.
- Davis, E.E.** & Villinger, H.W., 2006. Transient formation fluid pressures and temperatures in the Costa Rica forearc prism and subducting oceanic basement: CORK monitoring at ODP sites 1253 and 1255, *Earth planet. Sci. Lett.*, **245**, 232–244.
- DeMets, C.**, Gordon, R.G. & Argus, D.F., 2010. Geologically current plate motions, *Geophys. J. Int.*, **181**, 1–80.
- Dixon, T.H.**, Jiang, Y., Malservisi, R., McCaffrey, R., Voss, N., Protti, M. & Gonzalez, V., 2014. Earthquake and tsunami forecasts: relation of slow slip events to subsequent earthquake rupture, *Proc. Natl. Acad. Sci. USA*, **111**, 17 039–17 044.
- Fan, G.**, Beck, S.L. & Wallace, T.C., 1993. The seismic source parameters of the 1991 Costa Rica aftershock sequence: evidence for a transcurrent plate boundary, *J. geophys. Res.*, **98**, 15 759–15 778.
- Feng, L.**, Newman, A.V., Protti, M., Gonzlez, V., Jiang, Y. & Dixon, T.H., 2012. Active deformation near the Nicoya Peninsula, northwestern Costa Rica, between 1996 and 2010: interseismic megathrust coupling, *J. Geophys. Res. Solid Earth*, **117**, doi:10.1029/2012JB009230.
- Field, E.H.** *et al.*, 2014. Uniform California earthquake rupture forecast, version 3 (UCERF3)—The time-independent model, *Bull. seism. Soc. Am.*, **104**, 1122–1180.
- Gao, H.**, Schmidt, D.A. & Weldon, R.J., 2012. Scaling relationships of source parameters for slow slip events, *Bull. seism. Soc. Am.*, **102**, 352–360.
- Ghosh, A.**, Newman, A.V., Thomas, A.M. & Farmer, G.T., 2008. Interface locking along the subduction megathrust from b-value mapping near Nicoya Peninsula, Costa Rica, *Geophys. Res. Lett.*, **35**, doi:10.1029/2007GL031617.
- Global Earthquake Model (GEM)**, 2018. CCARA project: caribbean and Central America earthquake risk assessment, Retrieved June 25, 2024, from <https://www.globalquakemodel.org/project/ccara>
- Global Earthquake Model (GEM)**, 2023. CCARA project: caribbean and Central America earthquake risk assessment, Retrieved June 25, 2024, from <https://www.globalquakemodel.org/proj/ccara>
- González, Á.**, Gómez, J.B. & Pacheco, A.F., 2005. The occupation of a box as a toy model for the seismic cycle of a fault, *Am. J. Phys.*, **73**, 946–952.
- Gündel, F.**, 1986. *Seismotectonics of Costa Rica: an Analytical View of the Southern Terminus of the Middle America Trench*, Doctoral Thesis, Univ. St., Cruz, CA, USA.
- Gutenberg, B.** & Richter, C.F., 1944. Frequency of earthquakes in California, *Bull. seism. Soc. Am.*, **47**, 73–131. Retrieved from <https://pubs.geoscienceworld.org/ssa/bssa/article-pdf/34/4/185/2690674/BSSA0340040185.pdf>
- Hanks, T.C.** & Kanamori, H., 1979. A moment magnitude scale, *J. Geophys. Res. B Solid Earth*, **84**, 2348–2350.
- Hidalgo-Leiva, D.A.** *et al.*, 2023. The 2022 seismic hazard model for Costa Rica, *Bull. seism. Soc. Am.*, **113**, 23–40.
- Ide, S.**, Baltay, A. & Beroza, G., 2011. Shallow dynamic overshoot and energetic deep rupture in the 2011 Mw 9.0 Tohoku-Oki earthquake, *J. Geophys. Res. Solid Earth*, **332**, 1426–1429.
- Jara, J.**, Jolivet, R., Socquet, A., Comte, D. & Norabuena, E., 2024. Detection of slow slip events along the southern Peru—northern Chile subduction zone, *Seismica*, **3**, doi:10.26443/seismica.v3i1.980.
- Jiang, J.** *et al.*, 2022. Community-driven code comparisons for three-dimensional dynamic modelling of sequences of earthquakes and aseismic slip, *J. Geophys. Res. Solid Earth*, **127**, doi:10.1029/2021JB023519.
- Jiang, Y.**, Liu, Z., Davis, E.E., Schwartz, S.Y., Dixon, T.H., Voss, N., Malservisi, R. & Protti, M., 2017. Strain release at the trench during shallow slow slip: the example of Nicoya Peninsula, Costa Rica, *Geophys. Res. Lett.*, **44**, 4846–4854.
- Jiang, Y.**, Wdowinski, S., Dixon, T.H., Hackl, M., Protti, M. & Gonzalez, V., 2012. Slow slip events in Costa Rica detected by continuous GPS observations, 2002–2011, *Geochem. Geophys. Geosyst.*, **13**, doi:10.1029/2012GC004058.
- Jolivet, R.** & Frank, W.B., 2020. The transient and intermittent nature of slow slip, *AGU Adv.*, **1**, doi:10.1029/2019AV000126.
- Jolivet, R.**, Simons, M., Duputel, Z., Olive, J.A., Bhat, H.S. & Bletery, Q., 2020. Interseismic loading of subduction megathrust drives long-term uplift in Northern Chile, *Geophys. Res. Lett.*, **47**, doi:10.1029/2019GL085377.
- Kagan, Y.Y.** & Jackson, D.D., 2016. Earthquake rate and magnitude distributions of great earthquakes for use in global forecasts, *Geophys. J. Int.*, **206**, 630–643.
- Kanamori, H.** & Kikuchi, M., 1993. The 1992 Nicaragua earthquake: a slow tsunami earthquake associated with subducted sediments, *Nature*, **361**(6414), 714–716.
- Kano, M.** *et al.*, 2018. Development of a slow earthquake database, *Seismol. Res. Lett.*, **89**, 1566–1575.
- Kato, A.** & Ben-Zion, Y., 2021. The generation of large earthquakes, *Nat. Rev. Earth Environ.*, **2**, 26–39.
- Kobayashi, D.**, Lafemina, P., Geirsson, H., Chichaco, E., Abrego, A.A., Mora, H. & Camacho, E., 2014. Kinematics of the western Caribbean:

- collision of the Cocos Ridge and upper plate deformation, *Geochem. Geophys. Geosyst.*, **15**, 1671–1683.
- Kolarsky, R. & Mann, P., 1995. Structure and neotectonics of an oblique subduction margin, southwestern Panama, in *Geologic and Tectonic Development of the Caribbean Plate Boundary in Southern Central America*, pp. 1–349, ed. Mann, P., Geological Society of America.
- LaFemina, P. et al., 2009. Fore-arc motion and Cocos Ridge collision in Central America, *Geochem. Geophys. Geosyst.*, **10**, doi:10.1029/2008GC002181.
- Lee, S., Choi, E. & Scholz, C.H., 2023. Do subducted seamounts act as weak asperities?, *J. Geophys. Res. Solid Earth*, **128**, doi:10.1029/2023JB027551.
- Legrand, D., Tassara, A. & Morales, D., 2012. Megathrust asperities and clusters of slab dehydration identified by spatiotemporal characterization of seismicity below the Andean margin, *Geophys. J. Int.*, **191**, 923–931.
- Li, D. & Gabriel, A.A., 2024. Linking 3D long-term slow-slip cycle models with rupture dynamics: the nucleation of the 2014  $M_w$  7.3 Guerrero, Mexico earthquake, *AGU Adv.*, **5**, doi:10.1029/2023AV000979.
- Linkimer, L., Arroyo, I.G., Alvarado, G.E., Arroyo, M. & Bakkar, H., 2018. The national seismic network of Costa Rica (RSN): an overview and recent developments, *Seismol. Res. Lett.*, **89**, 392–398.
- Lücke, O.H. & Arroyo, I.G., 2015. Density structure and geometry of the Costa Rican subduction zone from 3-D gravity modelling and local earthquake data, *Solid Earth*, **6**, 1169–1183.
- Marshall, J.S., Fisher, D.M. & Gardner, T.W., 2000. Central Costa Rica deformed belt: kinematics of diffuse faulting across the western Panama block, *Tectonics*, **19**, 468–492.
- Matsumoto, S., Iio, Y., Sakai, S. & Kato, A., 2024. Strength dependency of frequency–magnitude distribution in earthquakes and implications for stress state criticality, *Nat. Commun.*, **15**, doi:10.1038/s41467-024-49422-7.
- Maubant, L., Frank, W.B., Wallace, L.M., Williams, C.A. & Hamling, I., 2023. Imaging the spatiotemporal evolution of plate coupling with interferometric radar (InSAR) in the Hikurangi subduction zone, *Geophys. Res. Lett.*, **50**, doi:10.1029/2023GL105388.
- McGuire, R.K., 1995. Probabilistic seismic hazard analysis and design earthquakes: closing the loop, *Bull. seism. Soc. Am.*, **85**, 1275–1284. Retrieved from <http://pubs.geoscienceworld.org/ssa/bssa/article-pdf/85/5/1275/5342611/bssa0850051275.pdf>
- Mescua, J.F. et al., 2017. Middle to late Miocene contractional deformation in Costa Rica triggered by plate geodynamics, *Tectonics*, **36**, 2936–2949.
- Michel, S., Jolivet, R., Jara, J. & Rollins, C., 2023. Seismogenic potential of the subduction zone in northern Chile, *Bull. seism. Soc. Am.*, **113**, 1013–1024.
- Michel, S., Jolivet, R., Rollins, C., Jara, J. & Dal Zilio, L., 2021. Seismogenic potential of the main Himalayan thrust constrained by coupling segmentation and earthquake scaling, *Geophys. Res. Lett.*, **48**, doi:10.1029/2021GL093106.
- Molnar, P., 1979. Earthquake recurrence intervals and plate tectonics, *Bull. seism. Soc. Am.*, **69**, 115–133.
- Montero, W., 1986. Períodos de recurrencia y tipos de secuencias sísmicas de los temblores interplaca e intraplaca en la región de Costa Rica, *Rev. Geol. Amér. Central*, **5**, 35–72.
- Montero, W., 2001. Neotectónica de la región central de Costa Rica: frontera oeste de la microplaca de Panamá, *Rev. Geol. Amér. Central*, **24**, 29–56.
- Montero, W., Lewis, J.C. & Araya, M.C., 2017. The Guanacaste volcanic arc sliver of northwestern Costa Rica, *Sci. Rep.*, **7**(1797), doi:10.1038/s41598-017-01593-8.
- Montero, W., Paniagua, S., Kussmaul, S. & Rivier, F., 1992. Geodinámica interna de Costa Rica, *Rev. Geol. Amér. Central*, **14**, 1–12.
- Morell, K.D., Fisher, D.M. & Gardner, T.W., 2008. Inner forearc response to subduction of the Panama Fracture Zone, southern Central America, *Earth planet. Sci. Lett.*, **265**, 82–95.
- Mortgat, C.P., Zsutty, T.C., Shah, H.C. & Lubetkin, L., 1977. *A Study of Seismic Risk for Costa Rica*, The John A. Blume Earthquake Engineering Center, Department of Civil and Environmental Engineering, Stanford, California. Retrieved from <http://blume.stanford.edu>
- Moya-Fernández, A., Pinzón, L.A., Schmidt-Díaz, V., Hidalgo-Leiva, D.A. & Pujades, L.G., 2020. A strong-motion database of Costa Rica: 20 yr of digital records, *Seismol. Res. Lett.*, **91**, 3407–3416.
- Nishikawa, T., Ide, S. & Nishimura, T., 2023. A review on slow earthquakes in the Japan Trench, *Prog. Earth Planet. Sci.*, **10**, doi:10.1186/s40645-022-00528-w.
- Nishikawa, T., Matsuzawa, T., Ohta, K., Uchida, N., Nishimura, T. & Ide, S., 2019. The slow earthquake spectrum in the Japan Trench illuminated by the S-net seafloor observatories, *Science*, **365**, 808–813.
- Obara, K. & Kato, A., 2016. Connecting slow earthquakes to huge earthquakes, *Science (1979)*, **353**(6296), 253–257.
- Outerbridge, K.C. et al., 2010. A tremor and slip event on the Cocos-Caribbean subduction zone as measured by a global positioning system (GPS) and seismic network on the Nicoya Peninsula, Costa Rica, *J. Geophys. Res. Solid Earth*, **115**, doi:10.1029/2009JB006845.
- Osawa, S., 2017. Long-term slow slip events along the Nankai trough subduction zone after the 2011 Tohoku earthquake in Japan, *Earth Planets Space*, **69**, doi:10.1186/s40623-017-0640-4.
- Pacheco, J.F., Quintero, R., Vega, F., Segura, J., Jiménez, W. & González, V., 2006. The  $M_w$  6.4 Damas, Costa Rica, earthquake of 20 November 2004: aftershocks and slip distribution, *Bull. seism. Soc. Am.*, **96**, 1332–1343.
- Pagani, M. et al., 2014. Openquake engine: an open hazard (and risk) software for the global earthquake model, *Seismol. Res. Lett.*, **85**, 692–702.
- Pagani, M., Johnson, K. & Pelaez, J.G., 2021. Modelling subduction sources for probabilistic seismic hazard analysis, *Geol. Soc. Spec. Publ.*, **501**, 225–244.
- Perry, M., Muller, C., Protti, M., Feng, L. & Hill, E.M., 2023. Shallow slow slip events identified offshore the Osa peninsula in southern Costa Rica from GNSS time series, *Geophys. Res. Lett.*, **50**, doi:10.1029/2023GL104771.
- Plata-Martinez, R. et al., 2021. Shallow slow earthquakes to decipher future catastrophic earthquakes in the Guerrero seismic gap, *Nat. Commun.*, **12**, doi:10.1038/s41467-021-24210-9.
- Porras, H., Mescua, J., Durán, P., Cascante, M., Giambiagi, L. & Müller, C., 2021. Changing tectonic regimes in the central Costa Rica forearc between the Paleogene and the present: insights from structural analysis and focal mechanisms, *J. Geodyn.*, **143**, doi:10.1016/j.jog.2020.101814.
- Protti, M., González, V., Newman, A.V., Dixon, T.H., Schwartz, S.Y., Marshall, J.S., Feng, L., Walter, J.I., Malservisi, R. & Owen, S.E., 2014. Nicoya earthquake rupture anticipated by geodetic measurement of the locked plate interface, *Nature Geoscience*, **7**(2), 117–121.
- Protti, M., Gündel, F. & McNally, K., 1994. The geometry of the Wadati-Benioff zone under southern Central America and its tectonic significance: results from a high-resolution local seismographic network, *Phys. Earth planet. Inter.*, **84**, 271–287.
- Radiguet, M., Cotton, F., Vergnolle, M., Campillo, M., Valette, B., Kosogludov, V. & Cotte, N., 2011. Spatial and temporal evolution of a long term slow slip event: the 2006 Guerrero Slow Slip Event, *Geophys. J. Int.*, **184**, 816–828.
- Radiguet, M., Cotton, F., Vergnolle, M., Campillo, M., Walpersdorf, A., Cotte, N. & Kosogludov, V., 2012. Slow slip events and strain accumulation in the Guerrero gap, Mexico, *J. Geophys. Res. Solid Earth*, **117**, doi:10.1029/2011JB008801.
- Rivas-Medina, A., Benito, B. & Miguel Gaspar-Escribano, J., 2018. Approach for combining fault and area sources in seismic hazard assessment: application in south-eastern Spain, *Natural Hazards and Earth System Sciences*, **18**, 2809–2823.
- Rojas, W., Cowan, H., Conrad, L., Dahle, A. & Bungum, H., 1993. Regional seismic zonation for Central America, A Preliminary Model, NORSAR report under the RESIS regional seismology project, Oslo, Norway.
- Rollins, C. & Avouac, J.P., 2019. A geodesy- and seismicity-based local earthquake likelihood model for Central Los Angeles, *Geophys. Res. Lett.*, **46**, 3153–3162.
- Ruiz, S., et al., 2014. Intense foreshocks and a slow slip event preceded the 2014 Iquique  $M_w$  8.1 earthquake, *Science (1979)*, **345**(6201), 1162–1165.
- Saux, J.P., Molitorni Bergman, E.G., Evans, E.L. & Loveless, J.P., 2022. The role of slow slip events in the Cascadia subduction zone earthquake cycle, *J. Geophys. Res. Solid Earth*, **127**, doi:10.1029/2021JB022425.

- Schellart, W.P.** & Rawlinson, N., 2013. Global correlations between maximum magnitudes of subduction zone interface thrust earthquakes and physical parameters of subduction zones, *Phys. Earth planet. Inter.*, **225**, 41–67.
- Scherbaum, F.**, Cotton, F. & Smit, P., 2004. On the use of response spectral-reference data for the selection and ranking of ground-motion models for seismic-hazard analysis in regions of moderate seismicity: the case of rock motion, *Bull. seism. Soc. Am.*, **94**, 2164–2185.
- Scholz, C.**, 1982. Scaling laws for large earthquakes: consequences for physical models, *Bull. seism. Soc. Am.*, **72**, 1–14.
- Scholz, C.H.** & Campos, J., 2012. The seismic coupling of subduction zones revisited, *J. Geophys. Res. Solid Earth*, **117**, doi:10.1029/2011JB009003.
- Scholz, C.H.**, 2015. On the stress dependence of the earthquake b value, *Geophys. Res. Lett.*, **42**, 1399–1402.
- Scotti, O.**, Visini, F., Faure Walker, J., Peruzza, L., Pace, B., Benedetti, L., Boncio, P. & Roberts, G., 2021. Which fault threatens me most? Bridging the gap between geologic data-providers and seismic risk practitioners, *Front. Earth Sci. (Lausanne)*, **8**, doi:10.3389/feart.2020.626401.
- Stirling, M.** et al., 2012. National seismic hazard model for New Zealand: 2010 update, *Bull. seism. Soc. Am.*, **102**, 1514–1542.
- Tavakolizadeh, N.**, Mohammadigheymasi, H., Visini, F. & Pombo, N., 2024. FaultQuake: An open-source python tool for estimating seismic activity rates in faults, *Comp. & Geosci.*, **191**, 105659. doi:10.1016/j.cageo.2024.105659.
- Thingbaijam, K.K.S.**, Mai, P.M. & Goda, K., 2017. New empirical earthquake source-scaling laws, *Bull. seism. Soc. Am.*, **107**, 2225–2246.
- Uchida, N.**, Linuma, T., Nadeau, R., Bürgmann, R. & Hino, R., 2016. Periodic slow slip triggers megathrust zone earthquakes in northeastern Japan, *Science (1979)*, **351**, 488–492.
- Visini, F.**, Valentini, A., Chartier, T., Scotti, O. & Pace, B., 2020. Computational tools for relaxing the fault segmentation in probabilistic seismic hazard modelling in complex fault systems, *Pure appl. Geophys.*, **177**, 1855–1877.
- Voss, N.**, Dixon, T.H., Liu, Z., Malservisi, R., Prott, M. & Schwartz, S., 2018. Do slow slip events trigger large and great megathrust earthquakes?, *Sci. Adv.*, **4**, 8472–8503.
- Voss, N.K.**, Malservisi, R., Dixon, T.H. & Prott, M., 2017. Slow slip events in the early part of the earthquake cycle, *J. Geophys. Res. Solid Earth*, **122**, 6773–6786.
- Wallace, L.**, Webb, S., Ito, Y., Mochizuko, K., Hino, R., Henrys, S., Schwartz, S. & Sheehan, A., 2016. Slow slip near the trench at the Hikurangi subduction zone, New Zealand, *Science (1979)*, **352**, 697–701.
- Wells, D.L.** & Coppersmith, K.J., 1994. New empirical relationships among magnitude, rupture length, rupture width, rupture area, and surface displacement, *Bull. seism. Soc. Am.*, **84**, 974–1002.
- Weng, H.** & Ampuero, J.P., 2022. Integrated rupture mechanics for slow slip events and earthquakes, *Nat. Commun.*, **13**, doi:10.1038/s41467-022-34927-w.
- Wesnousky, S.G.**, 1986. Earthquakes, quaternary faults, and seismic hazard in California, *J. geophys. Res.*, **91**, 12 587–12 631.
- Westbrook, G.**, Hardt, N. & Heath, R., 1995. Structure and tectonics of the Panama–Nazca boundary, in *Geologic and Tectonic Development of the Caribbean Plate Boundary in Southern Central America*, pp. 1–349, ed. Mann, P., Geological Society of America.
- Xie, S.**, Dixon, T.H., Malservisi, R., Jiang, Y., Prott, M. & Muller, C., 2020. Slow slip and inter-transient locking on the Nicoya megathrust in the late and early stages of an earthquake cycle, *J. Geophys. Res. Solid Earth*, **125**, doi:10.1029/2020JB020503.
- Xue, L.**, Schwartz, S., Liu, Z. & Feng, L., 2015. Interseismic megathrust coupling beneath the Nicoya Peninsula, Costa Rica, from the joint inversion of InSAR and GPS data, *J. Geophys. Res. Solid Earth*, **120**, 3707–3722.
- Yoder, M.R.**, Holliday, J.R., Turcotte, D.L. & Rundle, J.B., 2012. A geometric frequency-magnitude scaling transition: measuring  $b=1.5$  for large earthquakes, *Tectonophysics*, **532–535**, 167–174.
- Youngs, R.R.** & Coppersmith, K.J., 1985. Implications of fault slip rates and earthquake recurrence models to probabilistic seismic hazard estimates, *Bull. seismol. Soc. Am.*, **75**, 939–964.
- Zhou, P.** & Xia, S., 2020. Effects of the heterogeneous subducting plate on seismicity: constraints from b-values in the Andaman–Sumatra–Java subduction zone, *Phys. Earth planet. Inter.*, **304**, 106499. doi:10.1016/j.pepi.2020.106499.
- Zöller, G.**, 2024. Recurrence times of large earthquakes: assimilating the effect of seismic coupling into a renewal model, *Bull. seism. Soc. Am.*, **114**, 1754–1761.

## APPENDIX A: CATALOGUE OF SSEs IN COSTA RICA

**Table A1.** SSEs documented in Costa Rica and considered in this study for the seismic slip rate approach.

Nicoya peninsula						
Year	Start	End	Max. Slip (cm)	Duration (days)**	$M_w$	References
2000*	?	?	12	25.5	6.8	(Gao <i>et al.</i> 2012)
2003	Aug-03	Sep-03	3	30	6.6–7.2	(Jiang <i>et al.</i> 2012; Xie <i>et al.</i> 2020)
2005	Jul-05	Aug-05	3	30	6.6–7.2	(Jiang <i>et al.</i> 2012; Xie <i>et al.</i> 2020)
2007	May-07	Jun-07	12	30	6.8	(Outerbridge <i>et al.</i> 2010; Jiang <i>et al.</i> 2012; Xie <i>et al.</i> 2020)
2009	Oct-08	Apr-09	16	180	7	(Jiang <i>et al.</i> 2012; Xie <i>et al.</i> 2020)
2011	Mar-11	Apr-11	3	20	6.8	(Jiang <i>et al.</i> 2012; Xie <i>et al.</i> 2020)
2012	Aug-12	Sep-12	13.5	30	6.9	(Jiang <i>et al.</i> 2012; Voss <i>et al.</i> 2017; Xie <i>et al.</i> 2020)
2014	Mar-14	Apr-14	13.5	30	6.9	(Voss <i>et al.</i> 2017; Xie <i>et al.</i> 2020)
2015	Oct-15	Nov-15	20	30	6.9	(Voss <i>et al.</i> 2017; Xie <i>et al.</i> 2020)
2017	Oct-17	Nov-17	16	30	7.1	(Xie <i>et al.</i> 2020)
2019	Oct-19	Nov-19	13.5	30	6.9	(Xie <i>et al.</i> 2020)

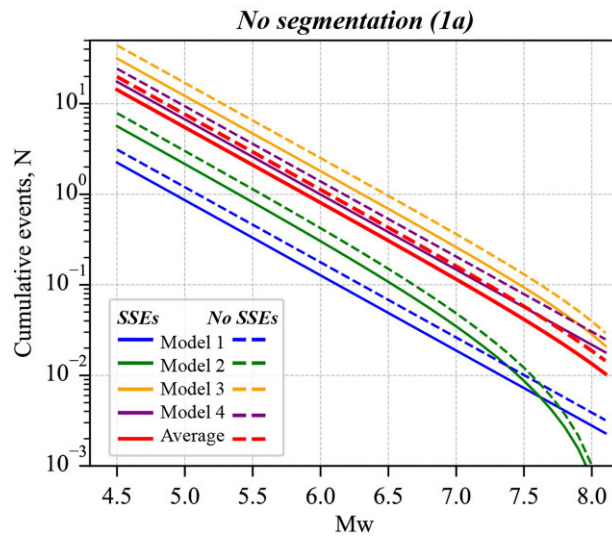
  

Osa peninsula						Reference
Year	Start	End	Max. Slip (cm)	Duration (d)	$M_w$	
2013*	2013	2013	15	30	6.5–6.7	
2018	Feb-18	Mar-18	30	30	6.7	
2018	Sep-18	Oct-18	15	30	6.5	(Perry <i>et al.</i> 2023)
2022	Feb-22	Mar-22	15	30	6.5	
2022	Apr-22	May-22	15	30	6.7	
2018	Sep-18	Oct-18	15	30	6.5	
2022	Feb-22	Mar-22	15	30	6.5	

\* Not well defined due to lack of instrumentation.

\*\* A 30-d duration is assumed when the exact event duration is unclear.

## APPENDIX B: MFD CHARACTERIZATION DETAILS

**Figure B1.** MFD for each of the four models used (Table 3) to convert from moment rates to earthquake rates and its average (used for the hazard computations), considering SSEs or not, without segmentation in the subduction interface (1a) (Fig. 4c).

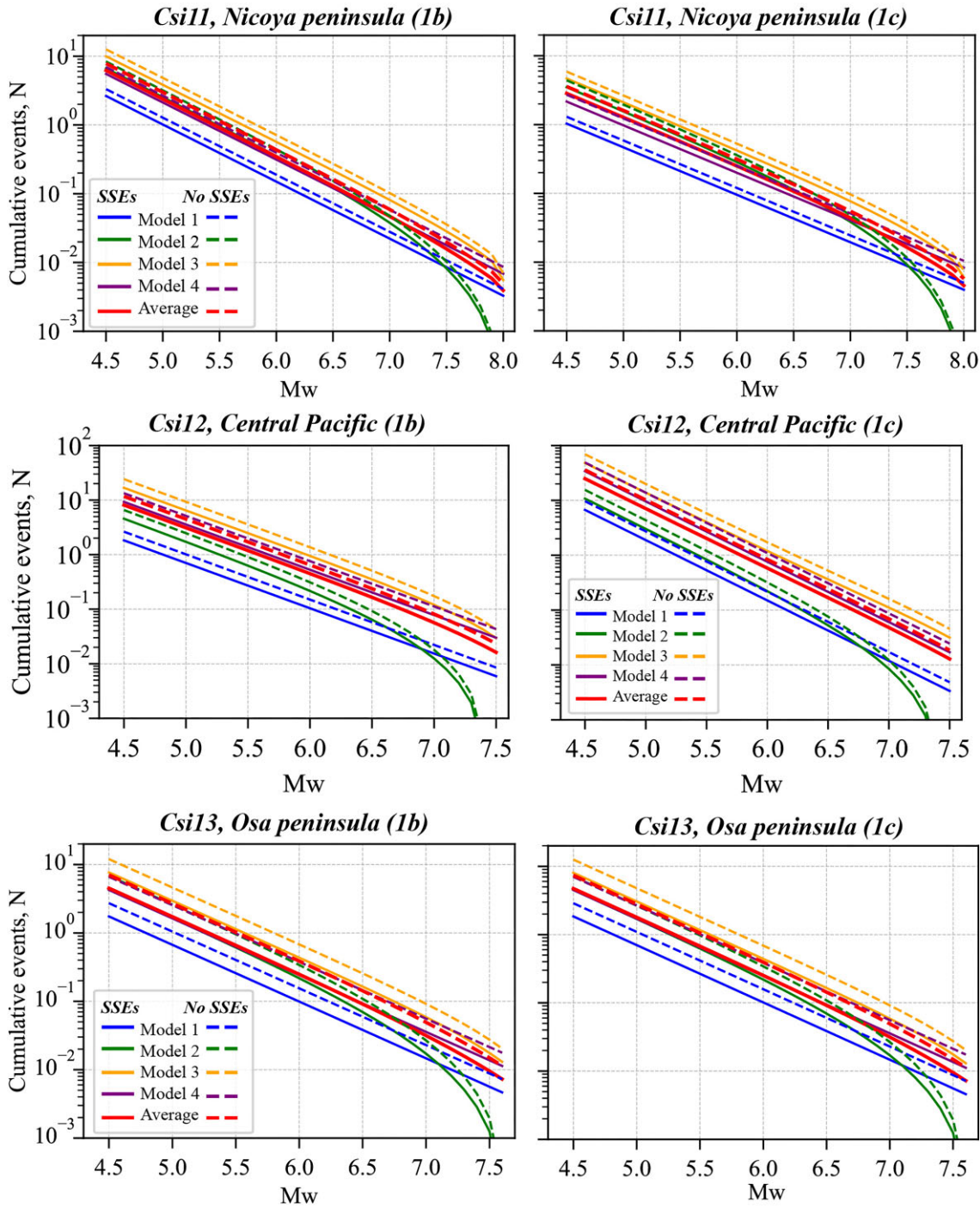


**Figure B2.** MFD for each of the four models used (Table 3) to convert from moment rates to earthquake rates and its average (used for the hazard computations), considering SSEs or not, using the segmentation along the interface with the different options of  $b$ -value explored (1b and 1c, Fig. 4c).

**Table B1.** MFD characterization based on geodetic information of the subduction interplate sources by different approaches considering and without considering SSEs and using  $M_w$  4.5 as  $M_{min}$  for the seismicity parameters calculation.

Seismic Source	Ia. Earthquake rates ( $N_{min}$ ) variation												2a. $M_{max}$ variation												
	Geometric characteristics						Without considering SSEs						Considering SSEs						Without considering SSEs						Considering SSEs
	Depth (km)	L (km)	W (km)	Dip (°)	Rake (°)	a-val	b-val	N <sub>min</sub>	M <sub>max</sub>	a-val	b-val	N <sub>min</sub>	M <sub>max</sub>	a-val	b-val	N <sub>min</sub>	M <sub>max</sub>	a-val	b-val	N <sub>min</sub>	M <sub>max</sub>	a-val	b-val	N <sub>min</sub>	M <sub>max</sub>
<b>a. Without segmentation using the general interpolate b-value for Costa Rica</b>																									
InterplateCosta Rica	12-35	~800	~52	~30	90	5.03	0.83	19.86	8.1	4.89	0.83	14.25	8.1	4.94	0.83	16.03	8.6	4.94	0.83	16.03	8.4				
<b>b. Using the general interpolate b-value in each segment</b>																									
Seismic Source	Ib. Earthquake Rates ( $N_{min}$ ) variation												2b. $M_{max}$ variation												Considering SSEs
	Geometric characteristics						Without considering SSEs						Considering SSEs						Without considering SSEs						Considering SSEs
	Depth (km)	L (km)	W (km)	Dip (°)	Rake (°)	a-val	b-val	N <sub>min</sub>	M <sub>max</sub>	a-val	b-val	N <sub>min</sub>	M <sub>max</sub>	a-val	b-val	N <sub>min</sub>	M <sub>max</sub>	a-val	b-val	N <sub>min</sub>	M <sub>max</sub>	a-val	b-val	N <sub>min</sub>	M <sub>max</sub>
Csi11	12-35	150	65	35	90	4.63	0.83	7.80	7.9	4.53	0.83	6.20	7.9	4.26	0.83	3.35	7.9	4.26	0.83	3.35	7.8				
Csi12	15-30	155	48	28	90	4.80	0.83	11.69	7.4	4.64	0.83	8.11	7.4	4.15	0.83	2.63	7.7	4.15	0.83	2.63	7.7				
Csi13	10-30	111	44	23	90	4.58	0.83	7.38	7.6	4.39	0.83	4.51	7.6	3.87	0.83	1.35	8.1	3.87	0.83	1.35	7.9				
<b>c. Using the b-value of the segment</b>																									
Seismic Source	Ic. Earthquake rates ( $N_{min}$ ) variation												2c. $M_{max}$ variation												Considering SSEs
	Geometric characteristics						Without considering SSEs						Considering SSEs						Without considering SSEs						Considering SSEs
	Depth (km)	L (km)	W (km)	Dip (°)	Rake (°)	a-val	b-val	N <sub>min</sub>	M <sub>max</sub>	a-val	b-val	N <sub>min</sub>	M <sub>max</sub>	a-val	b-val	N <sub>min</sub>	M <sub>max</sub>	a-val	b-val	N <sub>min</sub>	M <sub>max</sub>	a-val	b-val	N <sub>min</sub>	M <sub>max</sub>
Csi11	12-35	150	65	35	90	3.66	0.69	3.58	7.9	3.56	0.69	2.84	7.9	3.63	0.69	3.35	8.0	3.63	0.69	3.35	7.9				
Csi12	15-30	155	48	28	90	6.50	1.10	35.85	7.4	6.35	1.10	24.88	7.4	5.37	1.10	2.63	7.7	5.37	1.10	2.63	7.7				
Csi13	10-30	111	44	23	90	4.65	0.84	7.04	7.6	4.45	0.84	4.73	7.6	3.91	0.84	1.35	8.0	3.91	0.84	1.35	7.8				

$L$ , length;  $W$ , width;  $a$ -val,  $a$ -value;  $b$ -val,  $b$ -value;  $N_{min}$ , cumulative events from  $M_{min}$  ( $M_w$  4.5);  $M_{max}$ , maximum magnitude inferred.

## APPENDIX C: COMPLEMENTARY SEISMIC HAZARD COMPUTATIONS

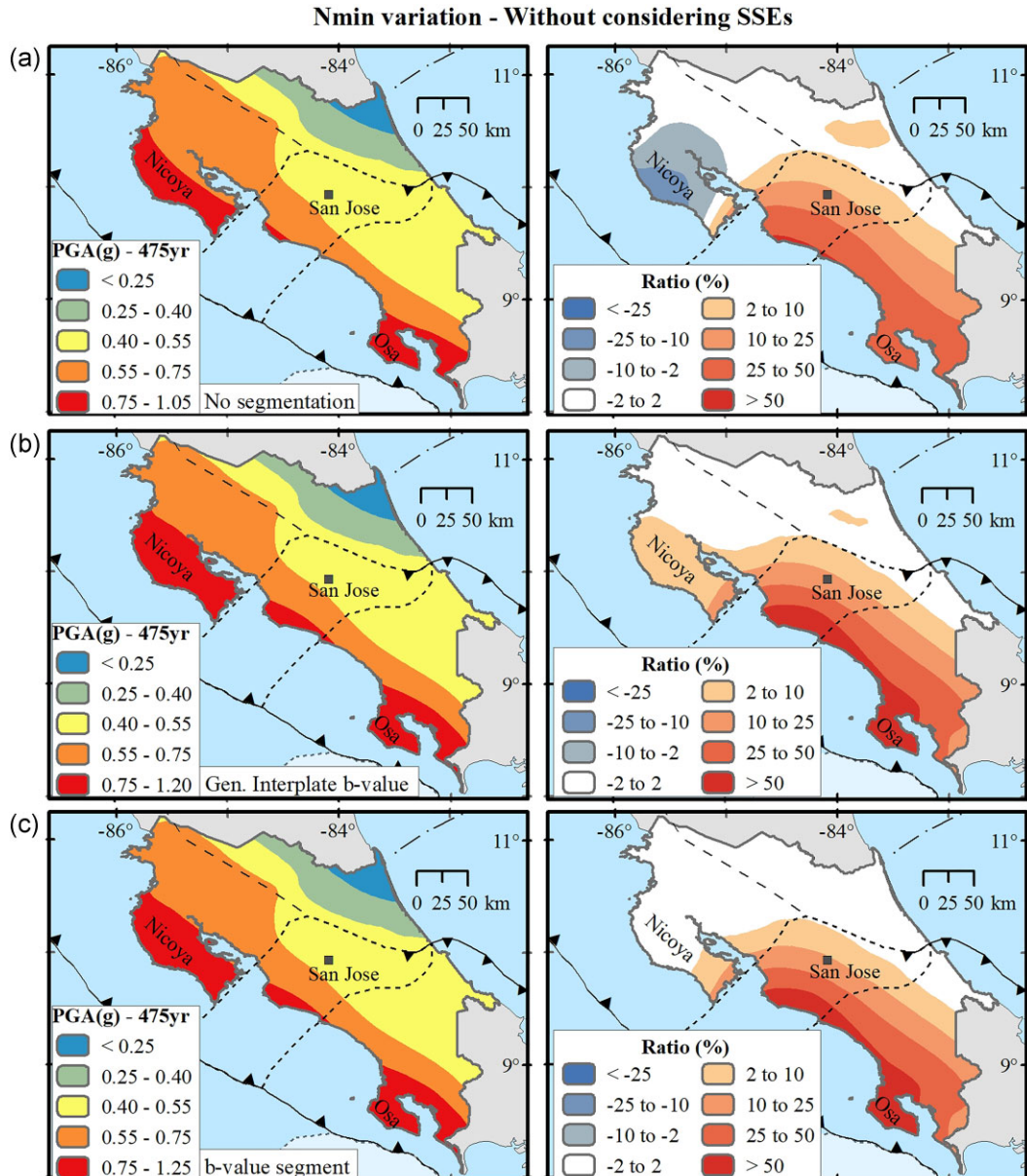


**Figure C1.** Seismic hazard computations without considering SSEs for the  $N_{\min}$  variation. (a) No segmentation. (b) Segmentation using the total interplate seismicity  $b$ -value. (c) Segmentation using the  $b$ -value of each segment. For each case, hazard and ratio maps (percentage of change with respect to the CRSHM 2022) are shown.

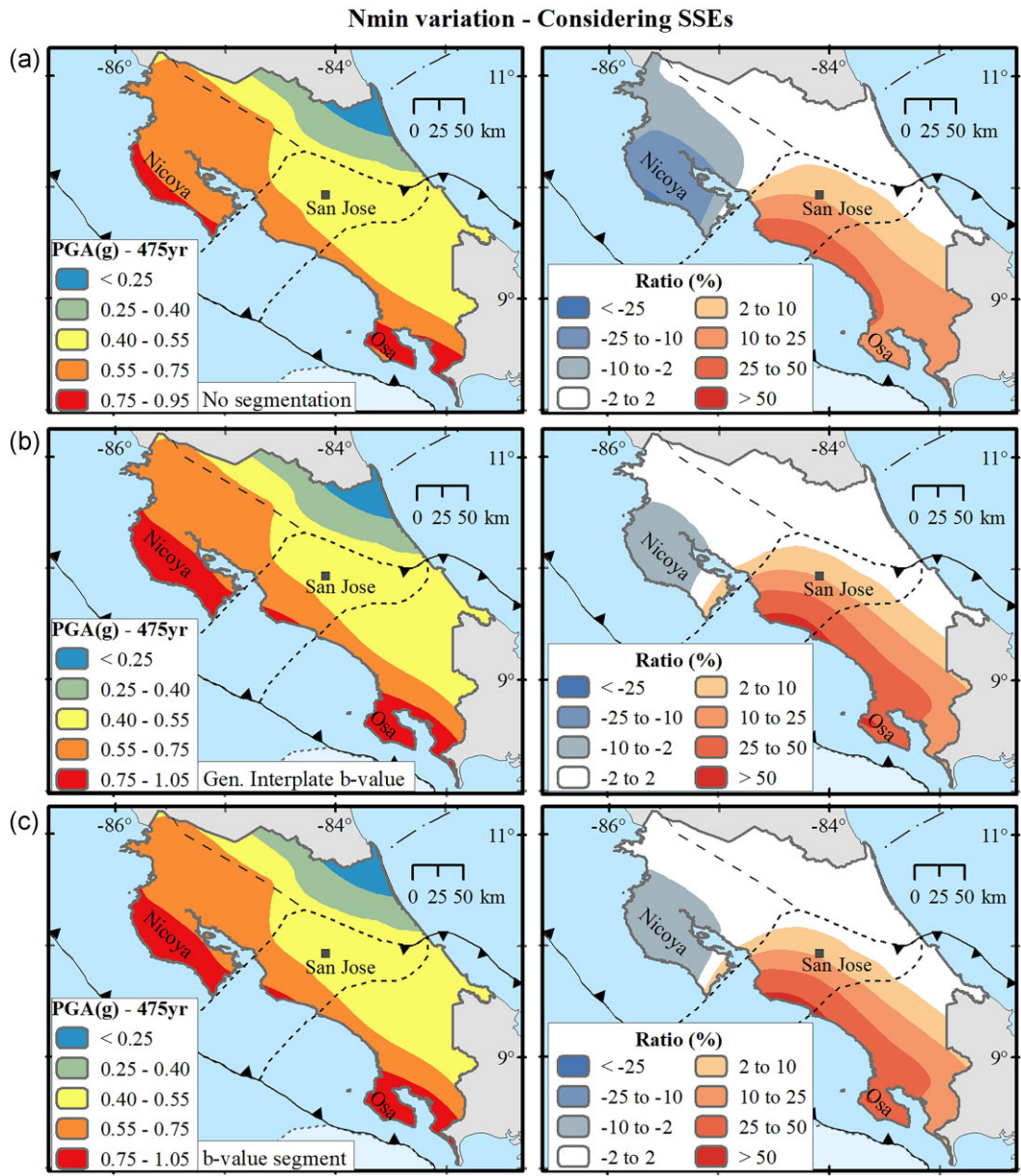


**Figure C2.** Seismic hazard computations considering SSEs for the  $N_{\min}$  variation. (a) No segmentation. (b) Segmentation using the total interplate seismicity  $b$ -value. (c) Segmentation using the  $b$ -value of each segment. For each case, hazard and ratio maps (percentage of change with respect to the CRSHM 2022) are shown.

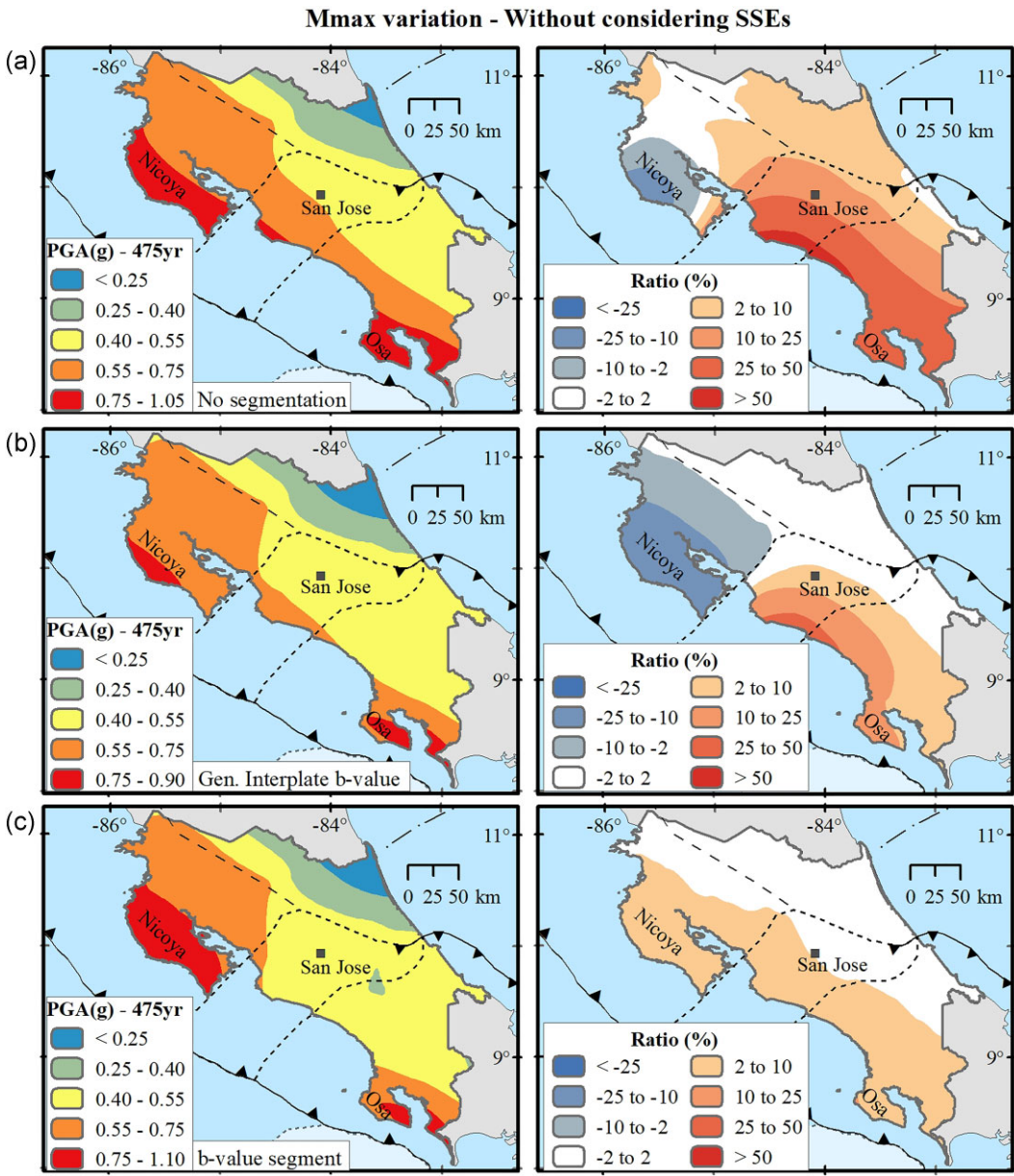


**Figure C3.** Seismic hazard computations without considering SSEs for the  $M_{\max}$  variation. (a) No segmentation. (b) Segmentation using the total interplate seismicity  $b$ -value. (c) Segmentation using the  $b$ -value of each segment. For each case, the hazard map and the ratio map (percentage of change with respect to the CRSHM 2022) are shown.

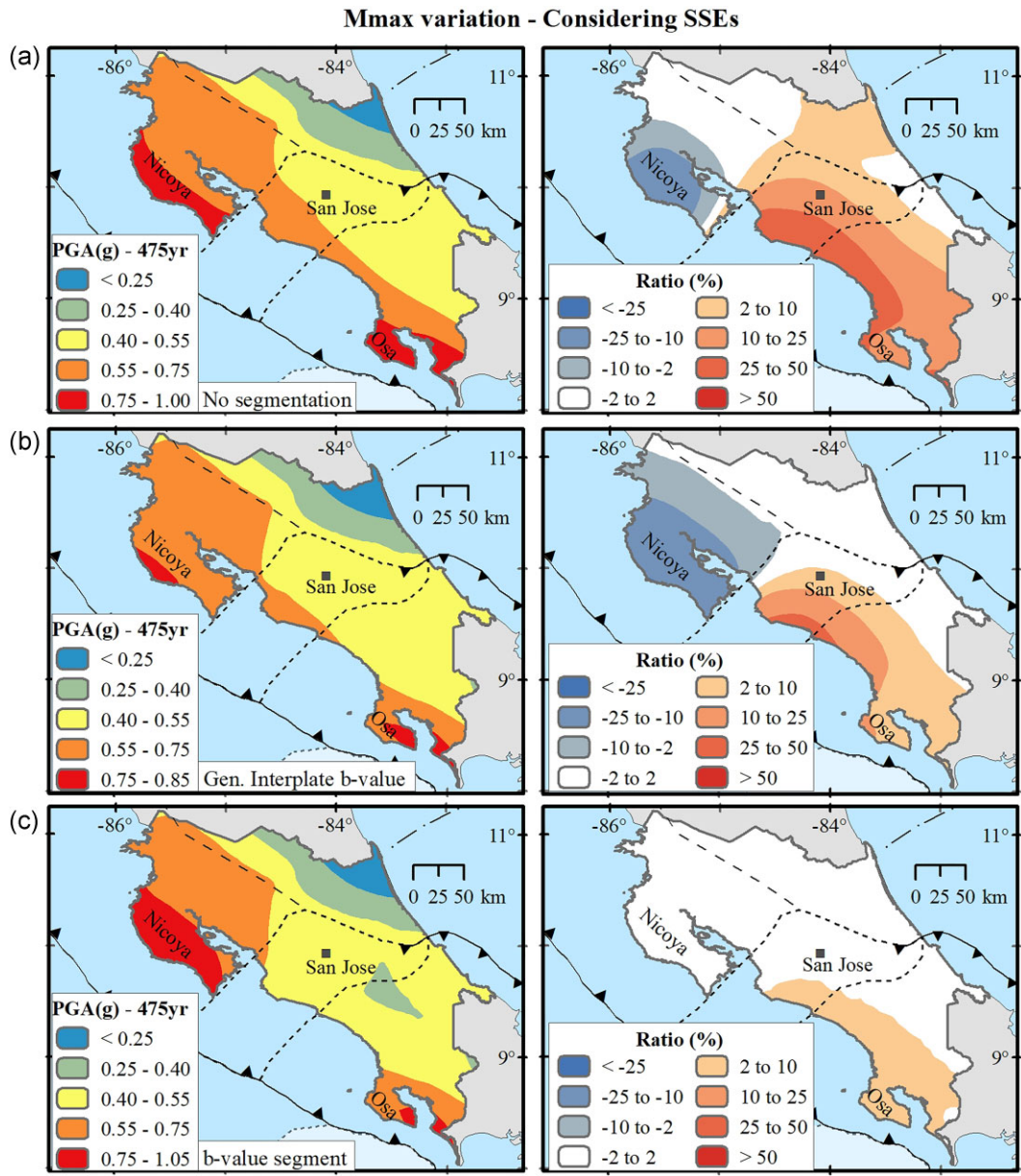


**Figure C4.** Seismic hazard computations considering SSEs for the  $M_{\max}$  variation. (a) No segmentation. (b) Segmentation using the total interplate seismicity  $b$ -value. (c) Segmentation using the  $b$ -value of each segment. In all cases, the ratio maps in percentage of change with respect to the CRSHM 2022.

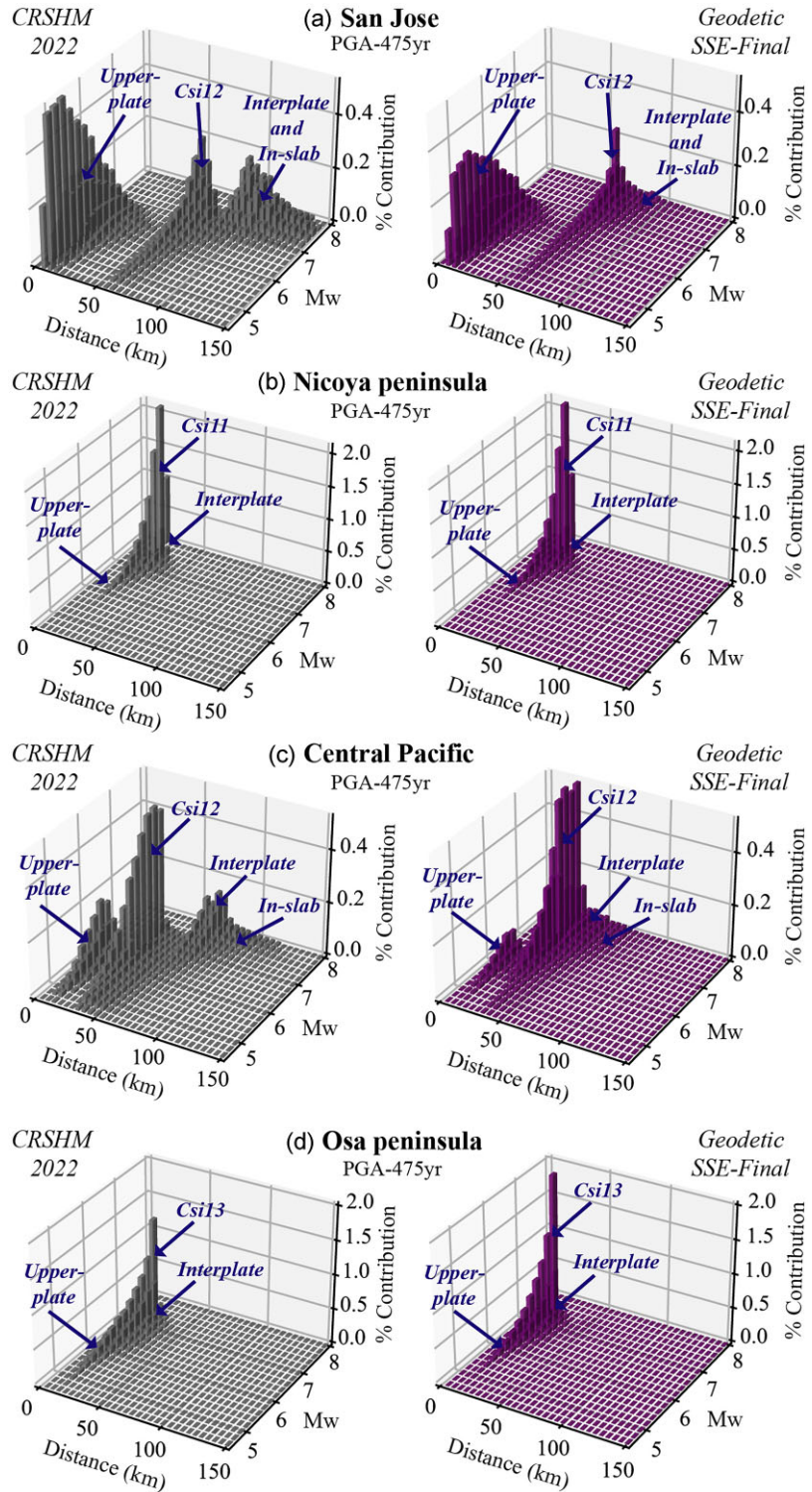


**Figure C5.** Seismic hazard disaggregation by distance-magnitude for the sites of interest. Results for the CRSHM 2022 (catalogue-based) and for this study (geodetic approach considering SSEs) for PGA and a return period of 475 yr: (a) San Jose, (b) Nicoya peninsula, (c) Central Pacific and (d) Osa peninsula. Arrows show seismic sources contributing the most to seismic hazard for each site (site locations are the same as in Fig. 11a).

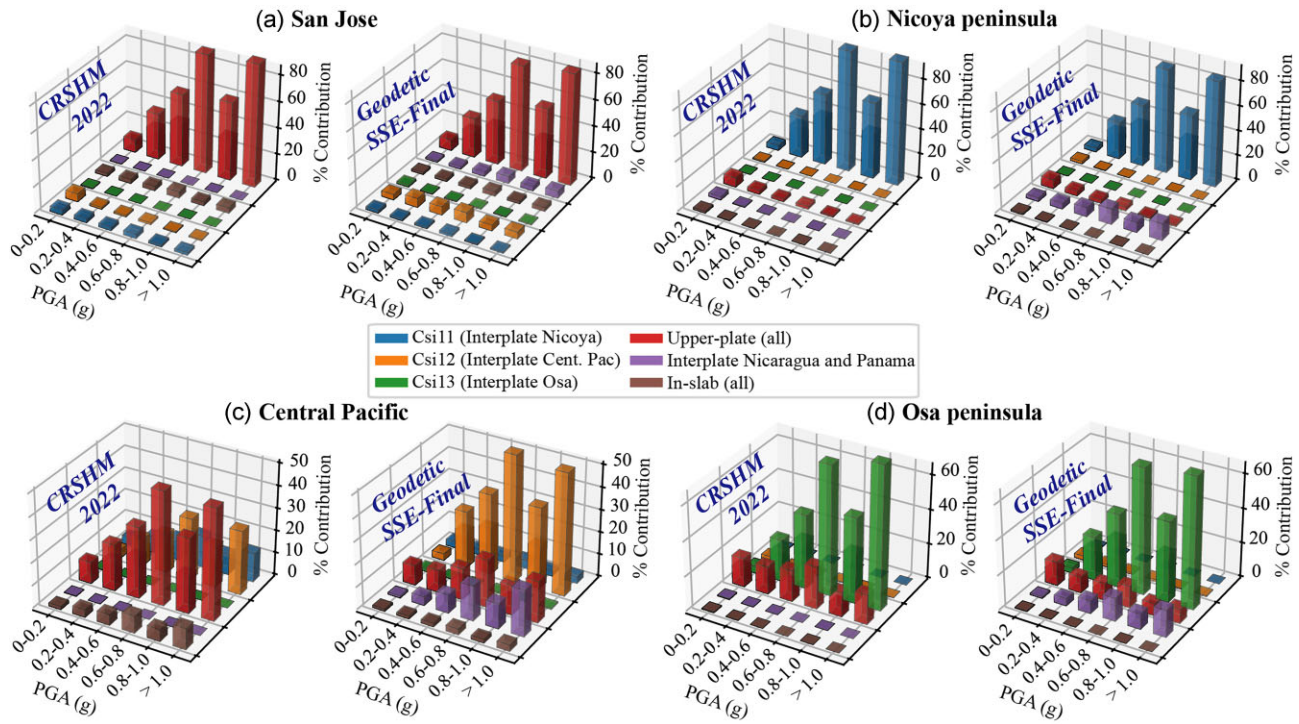


**Figure C6.** Seismic hazard disaggregation by source. Potential contribution of the sources to different peak ground accelerations according to its mean annual earthquake rates for CRSHM 2022 (catalogue-based) and for this study (geodetic approach considering SSEs) in: (a) San Jose, (b) Nicoya peninsula, (c) Central Pacific and (d) Osa peninsula (sites in Fig. 11a). Higher accelerations represent lower probability of exceedance and/or larger return periods.

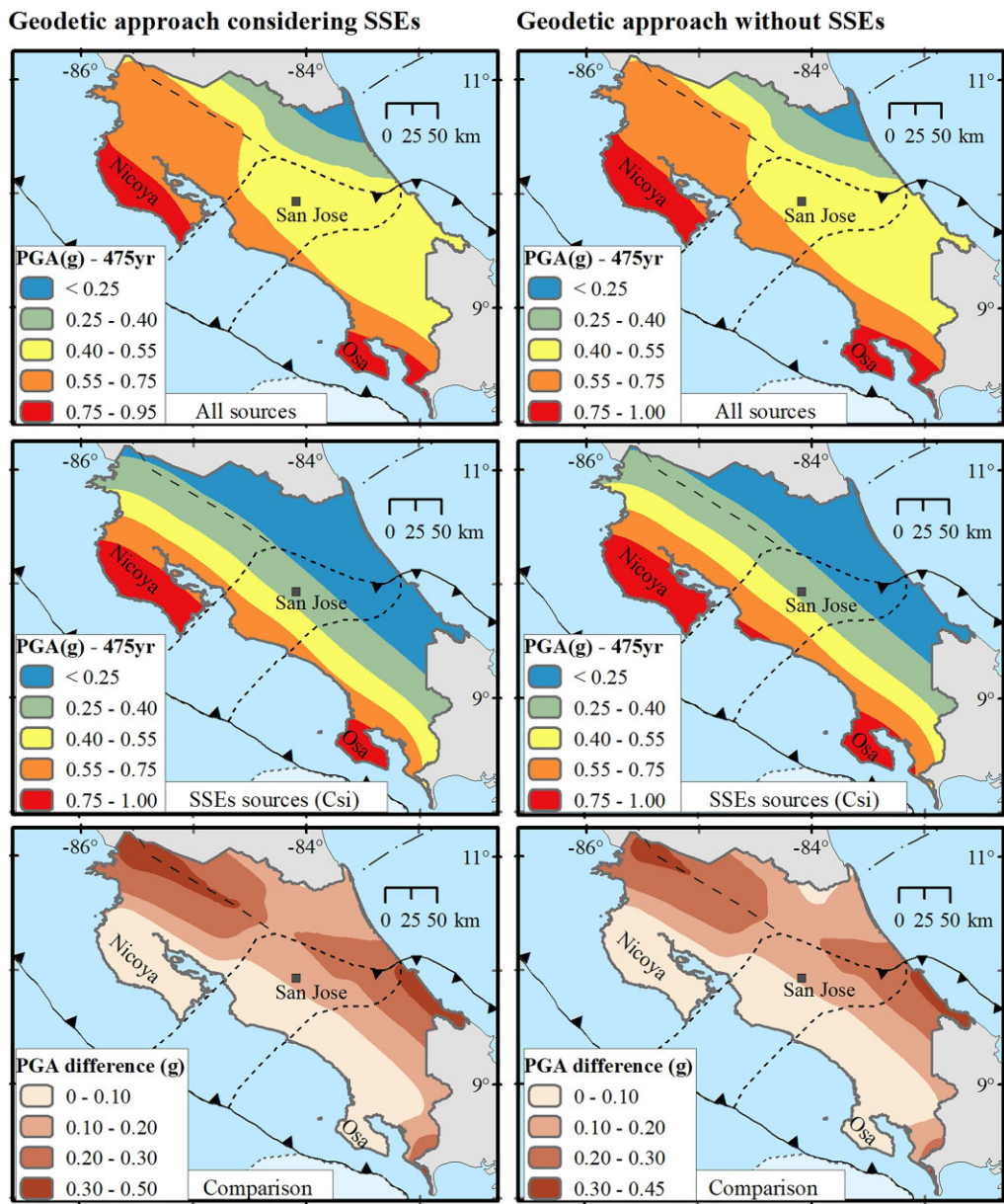


**Figure C7.** Comparison between hazard computations considering and without considering SSEs with all seismic sources of CRSHM 2022 and only with subduction interplate sources (Csi) for a return period of 475 yr.